






Cite this: *Chem. Soc. Rev.*, 2018, 47, 8438

# Catalysis by hybrid $sp^2/sp^3$ nanodiamonds and their role in the design of advanced nanocarbon materials

Yangming Lin,<sup>a,b</sup> Xiaoyan Sun,<sup>b</sup> Dang Sheng Su,<sup>b</sup> <sup>\*bc</sup> Gabriele Centi<sup>d</sup> <sup>d</sup> and Siglinda Perathoner<sup>e</sup> <sup>\*e</sup>

Hybrid  $sp^2/sp^3$  nanocarbons, in particular  $sp^3$ -hybridized ultra-dispersed nanodiamonds and derivative materials, such as the  $sp^3/sp^2$ -hybridized bucky nanodiamonds and  $sp^2$ -hybridized onion-like carbons, represent a rather interesting class of catalysts still under consideration. Their characteristics, properties and catalytic reactivity are presented, with an analysis of the state-of-the-art of their use in gas- and liquid-phase reactions, including photo- and electro-catalysis. It is remarked that intrinsic differences exist between these and other nanostructured carbon catalysts. The analysis shows how different features make nanocarbons unique with respect to other types of catalysts and are the bases for an advanced design of nanocarbon-type catalysts. The aspects discussed regard the presence of hybrid  $sp^2/sp^3$  configurations, nano-engineering related to the role of defects and vacancies in their catalytic behaviour, the creation of active sites by modification in the charge density at carbon atoms or C–C bonds, the generation of strained C–C bonds by curvature and other mechanisms, and the formation of semiconducting areas and defect sites at the interface with supported nanoparticles. The advanced strategies for identifying and quantifying active sites of carbon catalysts are highlighted.

Received 20th August 2018

DOI: 10.1039/c8cs00684a

rsc.li/chem-soc-rev

<sup>a</sup> Max-Planck-Institut für Chemische Energiekonversion, Stiftstraße 34-36, 45470, Mülheim an der Ruhr, Germany. E-mail: yang-ming.lin@cec.mpg.de

<sup>b</sup> Shenyang National Laboratory for Materials Science, Institute of Metal Research, Chinese Academy of Sciences, 72 Wenhua Road, Shenyang 110016, China

<sup>c</sup> Dalian Institute of Chemical Physics, Chinese Academy of Sciences, 457 Zhongshan Road, Dalian, China. E-mail: dssu@dicp.ac.cn

<sup>d</sup> University of Messina, ERIC aisbl and CASPE/INSTM, Dept.s MIFT – Industrial Chemistry, V.le F. Stagno D'Alcontres 31, 98166 Messina, Italy. E-mail: centi@unime.it

<sup>e</sup> University of Messina, Dept.s ChiBioFarAm – Industrial Chemistry, V.le F. Stagno D'Alcontres 31, 98166 Messina, Italy. E-mail: perathon@unime.it

## 1. Introduction

Nanocarbon-based catalysts have represented an area of increasing interest in recent years.<sup>1–30</sup> The term ‘nanocarbons’ defines materials where nano-dimensionality largely influences their characteristics and catalytic performances. Between the motivations of this interest<sup>15,31–35</sup> may be cited the facts that these materials (i) represent catalysts with characteristics different from classical types of materials, such as oxides,



Yangming Lin

Dr Yangming Lin received his PhD degree from the Institute of Metal Research, Chinese Academy of Sciences, in 2016, under the supervision of Prof. Dang Sheng Su and became a scientist at the Max-Planck-Institut für Chemische Energiekonversion (Germany). His main research interest is in the fabrication of carbon materials and semiconductor materials for catalysis and energy conversion.



Xiaoyan Sun

Dr Xiaoyan Sun obtained her PhD degree from the Institute of Metal Research, Chinese Academy of Sciences, in 2015 and became a Postdoc at Technische Universität Berlin (Germany). She has broad research interests in heterogeneous catalysis, materials chemistry and surface chemistry.



supported metals, zeolites and other types of micro/mesoporous materials, (ii) can be synthesized in a large variety of nanostructures, today often in a cost-competitive way, (iii) can be tuned by different modalities, particularly by doping and functionalization, and (iv) show often good conductivity characteristics, an essential property for the development of electrocatalysts and materials for energy, an area of growing relevance due to the on-going transition to a new energy and chemistry production.<sup>36,37</sup>

To address some of the demanding challenges arising from this transition, it is necessary to develop also disruptive catalysts,<sup>38</sup> i.e. catalysts that radically change the current concepts of catalysis and related reaction mechanisms, thus creating new

market opportunities and disrupting the existing ones. Nanocarbon-based materials, particularly those metal-free,<sup>24,35,39–41</sup> have many of the characteristics to be considered disruptive-type catalysts, because their reaction mechanism is often conceptually different from that present in current catalysts, for example in ODH (oxidative dehydrogenation) reactions.<sup>24</sup>

They can be synthesized in a variety of nanostructures (for example, carbon nano-fibres, -tubes, -coils, -horns, -diamonds, -onions, graphene, etc.) and dimensionalities, from nearly zero dimension (0D) (carbon nanodots), to 1D (nanotubes and nanofibers, and related classes of materials), 2D (graphene and graphene-like materials) and 3D (mesoporous carbons, and a large variety of 3D structures, such as exfoliated carbon structures, graphene scaffolds, hierarchical porous carbon foams, carbon nanofiber arrays).<sup>2,27,42–47</sup> In addition, their properties can be largely modified by doping and functionalization, and the creation of hybrid materials between different carbon nanostructures or with different catalytic elements, such as metals or metal-oxide nanoparticles.<sup>48–59</sup> Furthermore, they can host even isolated metal atoms, an area of increasing interest recently.<sup>60–67</sup>

Nanocarbons thus offer a wide range of possibilities for an advanced design of catalytic sites.<sup>68</sup> However, notwithstanding the relevant advances in their understanding as remarked in several reviews<sup>1–30</sup> in this area, there are still several aspects, which are underestimated.

A graphene sheet is the base structural element to understand the catalytic reactivity of nanocarbon materials. The carbon atoms in an ideal graphene sheet are essentially catalytically inactive due to their electronic structure. Only at the edges of graphene patches, where the symmetric structure is broken, are reactive sites present. This is somewhat similar to the catalytic chemistry of solid crystals, where the reactive sites are located at the edges, corners and similar coordinatively unsaturated sites. However, in nanocarbons, a larger number of possibilities are



**Dang Sheng Su**

*Prof. Dang Sheng Su completed his PhD at the Technical University of Vienna (Austria) in 1991, and moved to the Fritz-Haber-Institut der Max-Planck-Gesellschaft in the Department of Electron Microscopy. After a short stay at Hahn-Meitner Institut GmbH and Humboldt Universität zu Berlin (Germany) he joined the Fritz-Haber-Institut in 1999, where he worked on nanomaterials in heterogeneous catalysis and energy storage. He*

*was then Professor and Head of the Catalysis and Materials Division of the Shenyang National Laboratory for Materials Science, Institute of Metal Research, Chinese Academy of Sciences, and now is Professor in Physical Chemistry at the Dalian Institute of Chemical Physics, Chinese Academy of Sciences.*



**Gabriele Centi**

*Gabriele Centi is full professor of Industrial Chemistry at the University of Messina (Italy), President of IACS (International Association of the Catalysis Societies) and of ERIC aisbl (European Research Institute of Catalysis). He was the coordinator of the Network of Excellence on catalysis IDECAT and of several EU projects. He is Chair of the editorial board of ChemSusChem, and co-Editor in chief of the Journal of Energy*

*Chemistry (Elsevier) and of various book series. He was Chairperson of Europacat 2017 in Florence, Italy. He has published several reviews on catalysis and green energy, and he is author of over 450 scientific publications. The current h-index (Google Scholar) is 78 with about 22 500 citations.*



**Siglinda Perathoner**

*Siglinda Perathoner obtained her PhD in Chemical Science in 1988 working on the photophysics and photochemistry of supramolecular systems with V. Balzani and Nobel Laureate J. M. Lehn. In 2001 she joined the University of Messina and is associate professor of Industrial Chemistry presently. She has coordinated many EU projects. Among the awards and recognitions, the participation in 2011 to the "Nanolife" movie produced for the European*

*Commission to show to the public the results of nanotechnology. Her research interests include nanostructured oxides and nanocarbon materials for heterogeneous and photo- and electro-catalytic applications. The h-index (Google Scholar) is 63 with about 14 700 citations.*



present with respect to “classical” heterogeneous catalysts. In fact, in nanocarbons, the ideal symmetric electronic configuration can be broken by bending the ideal graphene sheet, as occurs, for example at the ends of carbon nanotubes (CNTs), where several local distortions, such as pentagonal or seven-membered rings, are necessary to minimize the energy necessary for the bending.

These defects are a key crucial aspect to understand the chemistry and catalytic reactivity of nanocarbons and are related to the possibility of easy change in the hybridization of carbon atoms, leading also to a large variety of structures possible in nanocarbons. In addition to defects where distortion leads to a rehybridization (for example, the formation of coupled C5 and C7 rings instead of a C6 ring, with consequent rehybridization between  $sp^2$  and  $sp^3$ ), more classical defects related to missing C-atom defects (for example, vacancies or dislocations) are possible. Although defect chemistry is present and relevant in other classes of catalysts, such as oxides, it is a more relevant aspect in nanocarbons due to the larger possibilities of the change in the hybridization of C-atoms.

Another important characteristic in nanocarbons, which again differentiates them from “classical” catalysts, is the possibility of doping with heteroatoms. O and N are the most common doping heteroatoms and can be introduced into nanocarbons to substitute C (inducing changes in the local coordination and hybridization) or to saturate dangling bonds. These heteroatoms are electronegative with respect to carbon, inducing consequently a rupture of the charge neutrality. Other types of heteroatoms, such as B, can instead accept electrons from carbon because of their valence of three, thus inducing a shift in the Fermi level of the conduction band.

These heteroatoms form functional reactive groups (aldehydic, acid, phenolic, chetonic, epoxy or quinone groups for oxygen doping, and quaternary N, pyridine, amine, or pyrrole for nitrogen doping, just as examples) which induce acid or redox catalytic functionalities, although often the different stabilities of these functional groups (by annealing or during the catalytic reaction) are not taken into proper account. In addition, the introduction of these heteroatoms induces local distortion in the structure of  $sp^2$ -hybridized carbons, thus inducing changes in the electron density at carbon atoms. Heteroatoms thus not only introduce reactive sites but also induce changes in the electronic local structure of the nanocarbons. Both aspects are relevant for the catalytic reactivity, although the second aspect is often underestimated.

There is thus rich catalytic chemistry deriving from doping with heteroatoms, which can be differentiated based on (a) reactive sites directly introduced (for example, Brønsted acid or redox sites) and (b) active sites deriving from the introduction of changes in the electronic structure of nearby carbon atoms. The latter include aspects such as Lewis acid–base sites, like pyridinic N and carbon atoms next to them (the electronegative nitrogen induces high positive charge density on adjacent carbon atoms).<sup>69</sup> While the first type of catalytic chemistry in nanocarbons has been extensively discussed, the second type of catalytic chemistry related to how the introduction of heteroatoms creates reactive carbon atoms has been

discussed in much less detail. In general, there is catalytic chemistry in nanocarbons related to the presence of reactive C sites related not only to dangling bonds, but also to the creation of reactive C atoms of C–C bonds associated with heteroatoms, defects, strains and curvature effects. In nanocarbons with hybrid  $sp^2/sp^3$  configurations, such as the nanodiamond family, it may be expected that this type of chemistry could be enhanced with respect to  $sp^2$ -type nanocarbons (like graphene, fullerenes, CNTs and derivatives). However, the catalytic chemistry of NDs and derivatives of this carbon family has been less studied with respect to other nanocarbon materials, and never reviewed in detail.

The scope of this review is thus to discuss the characteristics and catalytic behaviour of nanodiamonds and related materials to highlight how the results indicate the general role of reactive carbon sites in determining their catalytic behaviour, an aspect that we consider underestimated in understanding the possibilities opened by nanocarbons as novel catalytic materials.

## 2. Hybrid $sp^2/sp^3$ nanocarbons

Metal-free carbocatalysis<sup>1,24,35,39,40,49,70–76</sup> has inspired many studies in recent years, but most centred on the use of functional  $sp^2$ -type nanocarbons, such as graphene and CNT families. Less attention has been instead paid to other types of nanocarbon materials, particularly to  $sp^3$ -hybridized ultra-dispersed nanodiamonds (NDs) and their derivatives (UNDDs), including  $sp^3/sp^2$ -hybridized bucky nanodiamonds (BNDs) and  $sp^2$ -hybridized onion-like carbons (OLCs). They are emerging as a new category of the nanocarbon family, with interesting physicochemical properties, such as superior thermal and chemical stability, high surface energy, and unique  $\pi$  and  $\sigma$  bonding configurations. The latter aspects allow rich surface chemistry with characteristics not present in other nanocarbon materials.<sup>15</sup> These properties have made UNDDs competitive candidates for catalytic reactions besides conventional metal-based catalysts. In addition, they provide excellent materials to understand how the catalytic performance or the molecular structure and surface chemistry depend on the presence of hybrid  $sp^2/sp^3$  configurations rather than a predominantly  $sp^2$  configuration as in most of the nanocarbons reported in the cited studies. Current applications of UNDDs are mainly limited to their use as support, biocarrier, lubricant and fluorescent materials.<sup>77–81</sup>

Ultra-dispersed NDs are the raw materials for UNDDs. NDs have been found in interstellar dusts, meteorites and protoplanetary nebulae<sup>82</sup> and were first produced by a detonation method.<sup>83,84</sup> Different methods, such as chemical detonation, high-energy ball-milling of diamond microcrystals grown under high-pressure high-temperature conditions, laser ablation and plasma-assisted chemical vapor deposition (CVD), are now known to produce high  $sp^3$ -hybridized NDs. So far, chemical detonation has been the most cost-effective route to achieve large-scale production of NDs with high quality and uniform particle size (4–8 nm, the average value is about 5 nm,





as determined by HRTEM). The obtained NDs can be purified effectively using liquid oxidants (such as  $\text{HNO}_3$ , or  $\text{H}_2\text{SO}_4\text{-HNO}_3$  mixtures) and HCl to remove non-diamond carbon and trace metal impurities (Ag, Cu, Fe and other metals), respectively.<sup>81</sup> NDs produced in this way result in a high-purity metal-free carbon material.

## 2.1 Characteristics of UNDDs

**2.1.1 Structural characteristics of UNDDs.** The surfaces of NDs produced by detonation and further purified in strong oxidizing acids are covered with various oxygen groups and residual amorphous and disordered carbon.<sup>85,86</sup> Small-angle X-ray scattering (SAXS) patterns showed the core-shell-like structure of these ND particles,<sup>87</sup> with an average diameter of the core of  $\sim 30$  Å and shell thickness of  $\sim 8$  Å. The authors suggested the presence, together with the diamond core and the outer shell, of an amorphous carbon having mixed  $\text{sp}^2/\text{sp}^3$  bonding at the interface.<sup>87</sup>

High temperature annealing ( $T \leq 1500$  °C, vacuum or inert atmosphere) of NDs produces BNDs (Fig. 1), which are  $\text{sp}^2/\text{sp}^3$  hybrid materials with a  $\text{sp}^3$  carbon core covered with few  $\text{sp}^2$  graphite-like shells. Depending on the particle size and surface nature of original NDs, the number of graphitic shells of BNDs ranges from three to seven layers. BNDs combine the remarkable surface properties of graphitic materials with the characteristics of a diamond core. These promising hybrid materials have highly defective surfaces, high stability and a large presence of functional surface groups. BNDs can be further transformed into onion-like carbons (OLCs) at higher annealing temperature, generally  $> 1500$  °C (Fig. 1). OLC is an interesting non-planar self-enclosed graphitic material with

multiple layers of curved  $\text{sp}^2$  concentric shells (Fig. 1).<sup>88,89</sup> Detonation of NDs is the preferred method for the synthesis of large amounts of BNDs and OLCs at low cost.

X-ray diffraction (XRD) shows a significant (002) graphite peak for temperatures higher than 1100 °C, whose intensity increases with increasing annealing temperature, while the intensity of the (111) diamond peak decreases (Fig. 2a). The rate of phase transformation increases with temperature and the transformation is nearly complete for temperatures higher than 1500 °C, as illustrated by a small (111) diamond peak in Fig. 2a.

Raman spectroscopy is a powerful tool to characterize the structural transformations of NDs and their derivatives (UNDDs). Raman spectra of BNDs and OLCs annealed above 800 °C exhibit a G-mode ( $1585\text{ cm}^{-1}$ ) deriving from the vibration of carbon atoms in  $\text{sp}^2$ -hybridized carbon networks and a broad D-mode ( $1325\text{ cm}^{-1}$ ) correlated with the breathing of hexagonal carbon rings with defects (Fig. 2b). At lower synthesis temperatures, such as 800 °C and 1100 °C, the Raman spectra of the material resemble an amorphous carbon A-mode ( $\sim 1490\text{ cm}^{-1}$ )

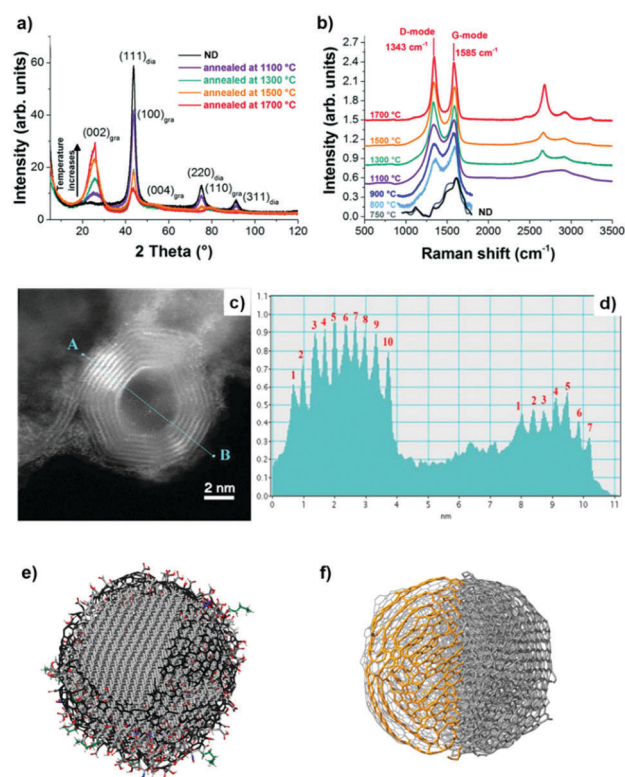


**Fig. 2** (a) XRD spectra and (b) vis Raman spectra of UNDDs annealed at different temperatures. (c) ADF-STEM image of an OLC and (d) the corresponding intensity profile. The difference in the number of graphitic shells is clearly shown. (e) Schematic model of a single  $\sim 5$  nm ND. The diamond core is covered with various oxygen groups and a thin layer of amorphous and disordered carbon, where  $\text{sp}^2$  carbon atoms are shown in black, oxygen atoms in red, and nitrogen in blue. The particles are stabilized by terminating the dangling bonds. Reproduced from ref. 88 with permission from Nature Publishing Group. (f) Schematic model of a single  $\sim 5$  nm OLC. Reproduced from ref. 89 and 90 with permission from Royal Society of Chemistry, copyright 2018.



**Fig. 1** Phase transformation from ND to OLC by annealing treatment together with HRTEM images and optical images of UNDDs, schematic illustrations of intermediate steps, and the assignment of possible physical effects depending on the annealing temperature. Reproduced from ref. 89 with permission from Royal Society of Chemistry, copyright 2016.





covering the surfaces of the particles, similar to the ND precursor. Due to the limited susceptibility of visible light excitation to insulating NDs, UV-Raman spectroscopy is often preferred. The diamond  $\text{sp}^3$ -mode and G-mode of NDs upon UV laser excitation are located at  $1336\text{ cm}^{-1}$  and  $1647\text{ cm}^{-1}$ , respectively.<sup>94</sup> When the synthesis temperature is  $800\text{ }^\circ\text{C}$ , the occurrences of the graphitic G-mode and the disordered D-mode derived from the ND precursor imply that the  $\text{sp}^3$ -hybridized carbon starts to transform into  $\text{sp}^2$ -hybridized OLC. The G-mode shows a relatively broad shape due to the large bond length variation in the material.

Higher annealing temperature or a longer annealing time will make the D- and G-modes sharper and lower the intensity of the secondary A-mode signal. For example, the  $I_{\text{D}}/I_{\text{G}}$  value of 1300 BND (calculated by the intensity ratio) decreases from 1.31 (4 h annealing) to 1.23 (8 h). The  $I_{\text{D}}/I_{\text{G}}$  value of the OLC decreases from 1.12 (4 h) to 1.02 (12 h).

The ADF-STEM image clearly shows the onion structure of the OLC (Fig. 2c and d). The corresponding intensity profile provides a direct and striking representation of the shell numbers (7–10 layers) of the OLC structure.<sup>90</sup> Mochalin and co-workers built the representative models of NDs and OLCs on the basis of the presence of surface functional groups and their variability,  $\text{sp}^2$  carbon and the shape of the particles (Fig. 2e and f).<sup>81</sup> After annealing at high temperature, the average particle size of OLCs does not change obviously and surface functional groups will be removed together with phase transformation.

In general, the thermal phase transformation of  $\text{sp}^3$ -hybridized NDs into  $\text{sp}^2$ -hybridized OLC involves a multistep process. It begins with the desorption of water and the detachment of surface oxygen functional groups from the NDs when heating up to around  $200\text{ }^\circ\text{C}$ . Upon increasing the temperature up to  $1300\text{--}1500\text{ }^\circ\text{C}$ , some functional groups like carboxyl, anhydride, and lactone groups are progressively removed with the formation of CO and  $\text{CO}_2$ . The dangling bonds on carbon atoms deriving from the progressive detachment of functional oxygen groups above  $800\text{ }^\circ\text{C}$  may further change with the formation of new  $\pi$ -bonds. The onset temperature of graphitization (namely, phase transformation) is typically in the  $800\text{--}900\text{ }^\circ\text{C}$  range. The HRTEM of BNDs further supports this indication. The phase transformation generates  $\text{sp}^2$ -hybridized carbon shells on the outside of the NDs, followed by continuous graphitization inside the particles.<sup>94</sup> Both the existing structural defects in ND surfaces and newly produced deriving from the detachment of surface functional groups increase the reactivity of surface carbon atoms and thus facilitate the phase transformation process.<sup>91</sup> For temperatures above  $1100\text{ }^\circ\text{C}$ , the initially highly disordered carbon shells become increasingly more graphitic with a lower defect density. A highly ordered OLC can be obtained when the temperature is above  $1500\text{ }^\circ\text{C}$ .

Therefore, by controlling the annealing temperature and time, the structural defect degree and surface oxygen groups of BNDs or OLCs can be easily tuned. The color of the UNDDs gradually changes from the gray of the NDs to black of the OLCs, as shown in the optical images of Fig. 1.

Two faces (111) and (110) of NDs have recently been considered to be the most likely starting points for phase transformation at elevated temperature, as described by Kuznetsov *et al.*<sup>92</sup> As shown in Fig. 3a, the graphitization process occurring at these two faces involves two steps: B/C or F/G. The binding energy per bond is found to be 2.75 eV for the (111) face and 3.92 eV for the (110) face, suggesting that graphitization of the (111) face is thermodynamically preferred over that of the (110) surface. The latter has to overcome a substantially higher barrier. It was proposed that the difference between interlayer binding energies over (111) and (110) originates from the different “packing” patterns of interlayer bonds in a volume between “parallel” planes. For the (111) planes, all such bonds are parallel in contrast to those of the (110) planes (B/C and F/G of Fig. 3a). More recently, as shown in Fig. 3b, the transformation of a ND particle into a large fullerene (like OLC) has been studied with the C–C bond rotation as the primary transformation step. The result shows a process of surface  $\text{sp}^2$  hybridization  $\rightarrow$   $\text{sp}^2$  C cage encapsulated diamond particle  $\rightarrow$  enlargement of the fullerene.<sup>93</sup>

Bragg coherent diffraction imaging (BCDI) was used for *in situ* study of the strain relaxation of NDs induced by annealing temperature (Fig. 3c). Before that, the selected NDs were drop-cast onto a (100)-surface-oriented silicon substrate. BCDI measurements were performed at a (111) Bragg peak of ND crystals at various temperatures in a helium environment. Upon increasing the temperature, the morphology and internal strain state of the NDs change, indicating the presence of lattice distortions and surface graphitization. The improvements in the homogeneity of the crystal lattice depend on the initial strain state. This method provides a direct 3D image to obtain intuitive understanding of the phase transformation of NDs into OLCs.<sup>94</sup> However, the detailed mechanism of transformation from an almost pure  $\text{sp}^3$  ND to a mixed  $\text{sp}^2/\text{sp}^3$  BND and then to a neat  $\text{sp}^2$  OLC is still not fully clear, despite also computational efforts.<sup>95–97</sup>

**2.1.2 Surface characteristics of UNDDs.** Osswald and co-workers proposed that aromatic carbons accounted for  $\sim 10\%$  of all carbons based on X-ray absorption near-edge structure spectroscopy results indicating about 6% of  $\text{sp}^2$ -hybridized carbon in pristine NDs produced by detonation.<sup>86</sup> The particles were stabilized by converting  $\text{sp}^3$  to  $\text{sp}^2$  carbon in the dangling bonds. The result of HRTEM already pointed out that the surface of the ND is engulfed by few layers of amorphous and disordered carbons (Fig. 1). Later, Cui *et al.* used a solid-state  $^{13}\text{C}$ -nuclear magnetic resonance ( $^{13}\text{C}$ -NMR) method to detect and quantify small amounts of  $\text{sp}^2$ -hybridized carbon, concluding that most of the  $\text{sp}^2$ -hybridized carbon is associated with C=O groups rather than aromatic-type carbon.<sup>98</sup> The content of the latter is only  $1.1 \pm 0.4\%$ .  $\text{sp}^3$ -Hybridized C–H and C–OH carbons, which cover most of the ND particle's surface, accounting for  $\sim 5\%$  each. The concentrations of C=O and –COOH groups were measured to be about 1.5%. Therefore, the total content of carbon (C–H, C–OH, C=O, and C=C groups) is up to 12–14% of all carbon, which matches the surface fraction expected for bulk terminated  $\sim 5\text{ nm}$  diameter ND particles.





**Fig. 3** (a) Phase transformation study of UNDDs using two-layer cluster modeling of the graphitization of diamond (111) and (110) faces, reprinted from ref. 92 with permission from the AIP Publishing, copyright 1999. (b) Transformation of a ND into a large fullerene (namely, OLC) simulated by the EDKMC method, reprinted from ref. 93 with permission from American Chemical Society, copyright 2014. (c) *In situ* Bragg coherent X-ray diffraction imaging (BCDI) reconstructions of two kinds of NDs (Crystals 1 and 2) at different stages during annealing, reprinted from ref. 94 with the AIP Publishing, copyright 2017.

The amount of surface oxygen groups of NDs approximates 9.8% as determined by XPS (Fig. 4a).<sup>99</sup> It can be fitted into carbonyl groups (C=O, 531.8 eV), carbon-oxygen ether-like single bonds (C-O, 532.8 eV) and phenolic groups (-OH, 533.7 eV). After annealing, the concentration of oxygen species of all BND samples decreases, however, higher than those of  $sp^2$ -hybridized reduced graphite oxide (GR, sample from Tanmei Ltd, China) and multi-walled carbon nanotubes (MWCNTs, sample from Shandong Dazhan Technology Ltd, China). Besides, it should be remarked that the specific characteristics of NDs largely depend on many aspects, such as the size, shape and synthesis as well as purification methods. The surface oxygen groups of NDs, including carboxylic acids, ketones, phenols and lactones, endorse the surface negative charge of the NDs over a pH range of 2–12.<sup>81</sup> Such abundant surface oxygen-terminated structures and potential disordered carbon shells provide the potential sites for catalysis.<sup>100–102</sup>

Using electron energy-loss spectroscopy (EELS), the  $sp^2$  content of the OLC is found to be about 96% (Fig. 4b and c). In addition, the  $sp^2$  graphitization degree of the OLC is much higher than those of GR (84%) and MWCNTs (80%). There is a good linear trend in the ND, BND and OLC series with respect to the surface area, which increases from 313  $m^2 g^{-1}$  (NDs) to about 460  $m^2 g^{-1}$  (OLC). The change in surface groups during the transformation of the NDs into OLC can be analysed by TPD. Generally, the thermal transformation of the NDs begins with the desorption of water and detachment of oxygen-containing surface functional groups from  $sp^3$ -hybridized carbon at around 200 °C. Further increase in the temperature to 700 °C will effectively remove functional groups such as carboxyl (-COOH, ~450 °C), anhydride (O=C-O-C=O, ~550 °C), ether (C-O-C, ~650 °C) and phenol (C-OH, ~700 °C) groups, with the formation of CO and CO<sub>2</sub> gases (Fig. 4d and e). When the annealing temperature is above 800 °C, only surface C=O remain.

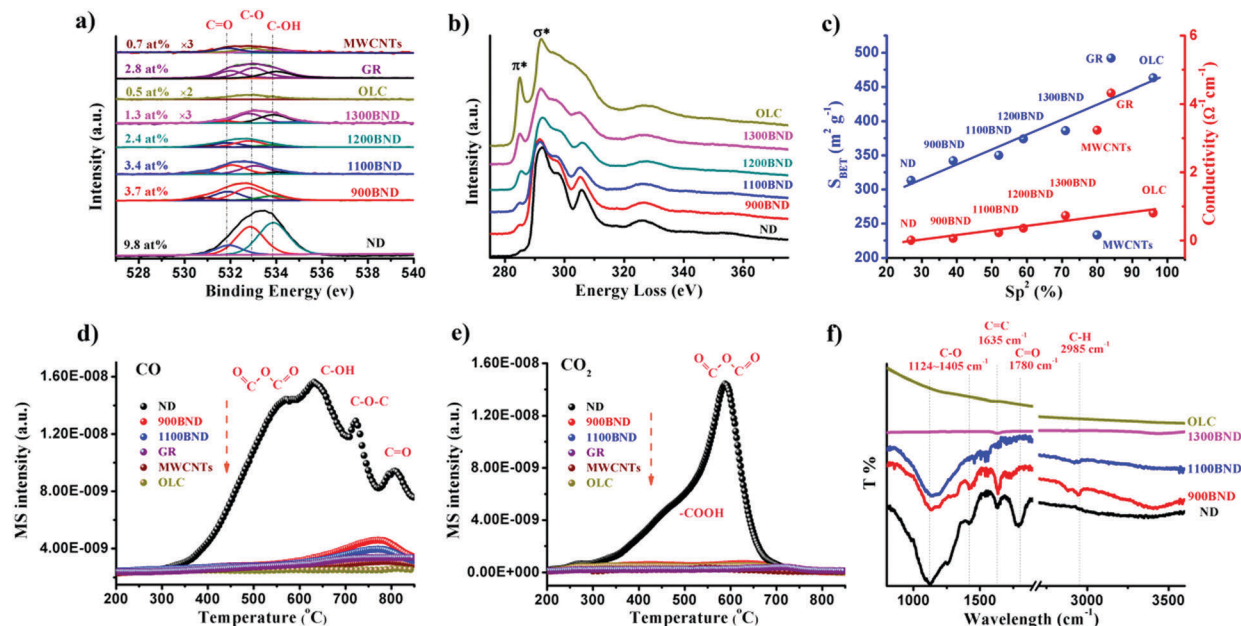


Fig. 4 (a) XPS O 1s spectra of representative carbon materials. (b) EELS spectra of UNDDs. (c) Specific surface area and conductivity in NDs and derived materials as functions of the relative fraction of  $sp^2$  carbon ( $sp^2$ , %). (d and e) TPD-CO (d,  $m/z = 28$ ) and TPD- $CO_2$  (e,  $m/z = 44$ ) profiles of various carbon materials in a He atmosphere using a heating rate of  $10\text{ K min}^{-1}$ . (f) FTIR spectra of UNDDs. Reproduced from ref. 99 with permission from Royal Society of Chemistry, copyright 2017.

The intense signals of CO and  $CO_2$  in the NDs indicate a large amount of oxygen functionalities with respect to other types of carbon materials.

The surface functional groups are also evidenced by FTIR. The spectrum of the NDs shows strong peaks due to the oxygen functional groups (Fig. 4f), in particular C-O ( $1124\text{--}1405\text{ cm}^{-1}$ ) and C=O ( $1780\text{ cm}^{-1}$ ) bands.<sup>103</sup> The red-shift and intensity weakening of the signal in the BNDs are attributed to its specific  $sp^3/sp^2$  structure and the minor amount of surface groups, respectively. The lack of bands associated with the oxygen functional groups in the OLC is related to the ordered  $sp^2$  carbon structure (96% graphitization degree) and the negligible amount of surface heteroatoms.

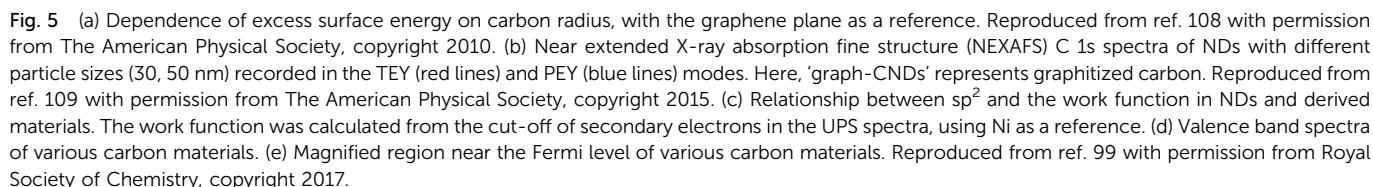
The thermal stability of UNDDs is extraordinary. Barnard and coworkers, by applying a model based on the calculated heat of formation, proposed that the thermostability of BNDs should range between the upper limit of fullerenes and the lower limit of NDs.<sup>104</sup> Costa *et al.* studied the standard enthalpies of formation at  $25\text{ }^\circ\text{C}$  in various nanocarbons obtaining the following ranking in thermostability: graphite > BNDs > NDs > SWCNTs > OLCs >  $C_{60}$ . The authors emphasized that the high stability of BNDs may be attributed to the oxygen-containing functional groups bonded to the  $sp^2$  structure.<sup>105</sup> It is worthy of note that the results of TGA indicate that the OLC exhibits the best thermostability and oxidation resistance among other nanocarbons under an Ar atmosphere and in air, as shown by the shift to higher temperatures of the start of weight losses. The oxidation onset temperature of the OLC in air reached  $600\text{ }^\circ\text{C}$ . Upon increasing the annealing temperature, the particle size of the UNDDs does not show changes related to structural rearrangement. A typical particle size of 4–8 nm is maintained.

**2.1.3 Electronic properties of UNDDs.** UNDDs have a unique electronic configuration in comparison to other nanocarbons due to their specific spherical structure and high curvature. Tomita and co-workers used electron spin resonance (ESR) to investigate the electronic properties of OLCs. They indicated that these materials are characterized by small graphitic  $sp^2$  domains (curved sheets, where  $\pi$  electrons are localized) terminating with dangling bond defects.<sup>106</sup> Bulush-eva *et al.* showed by X-ray emission spectroscopy and theoretical calculation that OLCs, compared to NDs and BNDs, have an enhanced localization of weakly bonding electrons as a result of holed defect structures in curved graphitic networks.<sup>107</sup> Moreover, using theoretical calculation, an inverse relationship between the excess surface energy and the radius of carbon materials was determined.<sup>108</sup> As shown in Fig. 5a, OLC with 5 nm diameter exhibits a higher surface energy ( $\sim 0.018\text{ eV per bond}$ ) induced by curvature than the graphene plane and SWCNTs, making the OLC a stable material with an active surface. In addition, the electrical conductivity of UNDDs improves from 0.011 (NDs) to  $0.802\text{ (OLCs)}\ \Omega^{-1}\text{ cm}^{-1}$ , as shown in Fig. 3c, although these values are lower with respect to those for highly ordered pyrolytic graphite (HOPG), MWCNTs and graphitic carbon (GR). Compared with NDs and BNDs, we can assume an increased electrical conductivity for OLCs synthesized at higher temperatures because of enhanced carbon ordering, as confirmed by the literature.<sup>108</sup>

The electronic structures of NDs with different particle sizes were studied with near extended X-ray absorption fine structure (NEXAFS, Fig. 5b).<sup>109</sup> The absorption structure at A2 at a photon energy of  $\sim 288.6\text{ eV}$  was regarded as a result of the  $C\ 1s \rightarrow \pi(C=O)$  transitions in carbonyl or carboxyl groups, CO or COOH.







energy) due to the significant curvature of the graphitic shell, rather than to surface functional groups or the  $\text{sp}^2$  content of the nanocarbons.<sup>113–115</sup> The effects of curvature on the work function in the case of CNTs have been previously reported.<sup>115</sup>

**2.2.1 Gas-phase reactions.** Metal-free nanocarbons are potential alternatives to conventional metal-based catalysts in some industrially important reactions.<sup>116–118</sup> Direct dehydrogenation (DH) and oxidative dehydrogenation (ODH) reactions (to produce olefins) are one of the major applications of UNDD catalysts. The DH reaction involves direct removal of hydrogen atoms from hydrocarbons to form relevant alkenes. It normally requires high reaction temperatures, being a reversible endothermic reaction. This process inevitably produces carbon deposits that could lead to the deactivation of the catalyst used. In contrast, the ODH reaction is an irreversible exothermic transformation and can be operated at a lower temperature, but with the loss of selectivity due to carbon oxide formation.

Typically, the catalysts used in DH and ODH reactions are transition metals and metal oxides, such as  $\text{Fe}_2\text{O}_3$ , Pt,  $\text{Cr}_2\text{O}_3$ ,  $\text{V}_2\text{O}_5$ ,  $\text{MoO}_x$ ,  $\text{Ga}_2\text{O}_3$ -based catalysts, and so on.<sup>119,120</sup> To date, various hydrocarbons have been tested by DH or ODH using UNDDs or doped UNDDs, including ethylbenzene (EB),<sup>121–125</sup> *n*-butane,<sup>126</sup> propane<sup>127–130</sup> and methane.<sup>131</sup> Due to their unique structure and surface properties, UNDDs and doped UNDDs not only exhibit a superior catalytic activity to other carbon materials, but in some cases they also provide even better performances than conventional metal-based catalysts. However, it is beyond the scope here to show that NDs and related materials are commercially better catalysts for these reactions. We will remark here on only their interesting

catalytic chemistry related to the peculiar structure, surface and electronic properties of UNDDs discussed in the previous section.

**2.2.1.1 DH reactions catalyzed by UNDDs.** Zhang *et al.* reported excellent catalytic performance of NDs in EB dehydrogenation to styrene under steam-free conditions,<sup>125</sup> superior to that of a commercial iron oxide catalyst used as reference, whose activity decreased rapidly from 20.2 to 9.2% within 2 h due to surface fouling by carbonaceous deposits. NDs show an activity nearly three times higher with respect to iron oxide and stable even after 60 h stream time (Fig. 6a). Note, however, that this K-promoted iron oxide used as reference was originally developed for DH of ethylbenzene strongly diluted with steam. It was also found that the ND catalyst is several times more active and selective than other nanocarbon materials such as nanographites, MWCNTs, and mesoporous carbons (Fig. 6b). *In situ* XPS and DRIFT tests show that the fraction of  $\text{O}=\text{C}$  (at 530.9 eV) decreases with parallel increase of  $\text{O}-\text{C}$  (at 532.9 eV), suggesting the reduction of  $\text{C}=\text{O}$  to  $\text{C}-\text{OH}$  by the hydrocarbon and a possible relationship between ketonic  $\text{C}=\text{O}$  species and the dehydrogenation reaction (Fig. 6c).

*In situ* DRIFT shows that the  $\alpha$ - or  $\beta$ -H of ethylbenzene interacts with ketonic O atoms, as evidenced by a significant red-shift from 1790 to 1765  $\text{cm}^{-1}$ , while the benzene nucleus is mostly skewed to the surface. Besides, vibrations of the benzene nucleus of EB do not change, similar to those in the gas phase (Fig. 6d). It is thus suggested that unsaturated ketone/diketone-type carbonyl groups ( $\text{C}=\text{O}$ ) have substantial

electron density at the oxygen atom, and thus can serve as Lewis bases to activate saturated hydrocarbons. Later, it was reported that BNDs with different graphitized degrees ( $\text{sp}^2/\text{sp}^3$  carbon ratios) have distinct reactivity in the DH of propane.

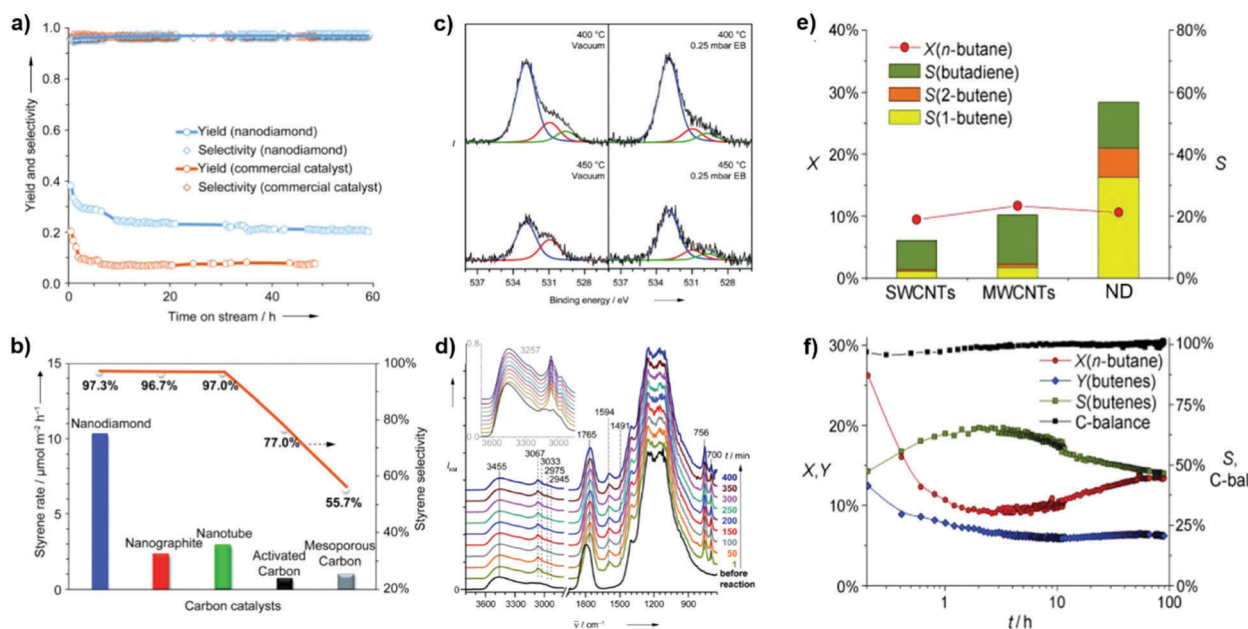
The unique structural defects of the  $\text{sp}^2/\text{sp}^3$  hybridized BND structure are likely responsible for the enhanced activation rate in propane dehydrogenation.<sup>128</sup>

The DH of methane, which is usually referred to as catalytic methane decomposition, has been often indicated as a valuable route to produce  $\text{CO}_x$ -free hydrogen.<sup>132</sup> In this case, carbon atoms from methane are completely transformed into a carbonaceous solid which may be eventually used. Although transition metal catalysts produce gaseous products with high initial hydrogen concentration,<sup>133–135</sup> their activity rapidly decreases due to the surface deposition of carbon.

Zhong *et al.* made an in-depth study on the metal-free catalysed CMD process using UNDDs as novel catalysts.<sup>131</sup> NDs show superior activity and stability with respect to other carbon materials, including activated carbon (AC), SWCNTs and MWCNTs. The catalytic activity was largely dependent on the defective sites in the graphene sheets of UNDDs.

The possible mechanism was proposed by theoretical simulation as a series of surface stepwise dissociation reactions of  $\text{CH}_x$  ( $x = 1-4$ ) to form layered graphene and molecular  $\text{H}_2$ .

**2.2.1.2 ODH reactions catalyzed by UNDDs.** The poor alkene selectivity is the major issue in the ODH reaction, even though much effort has been made towards understanding the alkane activation process. Keller and co-workers reported for the first



The high activity of NDs in the endothermic DH reaction may be attributed also to the very high thermal conductance of the  $\text{sp}^3$  phase at the core. It improves the heat-transfer efficiency close to the active sites on the surface.



For the ODH reaction of *n*-butane, the great difference in the selectivity between CNTs (MWCNTs, SWCNTs; see Fig. 6e) and NDs suggests that the well-graphitized surface strongly enhances the selective alkane activation owing to the controllable activation of oxygen. It was found that the surfaces of the NDs tend to transform into three to ten layers of graphitic shells during the *n*-butane ODH reaction. This transformation process from the  $sp^3$  to  $sp^2$  configuration can selectively generate the quinoidic carbonyl groups and effectively suppress the formation of electrophilic oxygen species. The electrophilic oxygen species are believed to be responsible for the combustion of alkenes on the carbon surface,<sup>117</sup> thus resulting in a higher product selectivity to the target butenes.

*2.2.1.1.4 Structural effects of UNDDs on the catalytic activity.* NDDs with different surface hybridized configurations ( $\text{sp}^3$ ,  $\text{sp}^3/\text{sp}^2$  and  $\text{sp}^2$ ) show different electronic states (Fig. 5c–e) and surface properties (Fig. 4). These differences reflect in the different natures of defects and anchored oxygen groups. For example, NDs and OLCs (as representative  $\text{sp}^3$ - and  $\text{sp}^2$ -hybridized structures of UNDDs) follow different ODH pathways for EB, even though they have similar sizes and shapes.<sup>124</sup> In the case of NDs, the  $\text{sp}^3$  carbon surface initially induces C–C bond cleavage and benzene formation, while the main reaction pathway would turn into styrene formation in parallel with the formation of  $\text{sp}^2$  carbons on the ND surface, which resulted in similar styrene selectivity to OLCs.

The significant role of structural transformation on the UNDD surface for catalytic activity and selectivity can be demonstrated also in the ODH of propane. By systematically controlling the formation of graphitic shells on NDs *via* the annealing treatment, which resulted in UNDDs with different  $sp^2/sp^3$  ratios, a good linear relationship between the  $sp^2$ -hybridized carbon fraction and the reactivity of the *in situ* formed surface oxygen species can be found in the ODH of propane.<sup>127</sup> For different hybridized nanostructures of UNDDs, the catalytic capabilities of the same types of active oxygen groups generated during the reaction depend on the  $sp^2$ -hybridized carbon fraction. The active oxygen groups formed on a graphitic OLC surface could provide 20% higher propene selectivity than that of an initial ND catalyst (Fig. 7). In addition, 30% higher selectivity than traditional  $sp^2$ -hybridized MWCNTs gives evidence that the unique curved and strained graphitic surfaces of the UNDDs were essential for the selective alkane activation.

For the DH reaction of propane, Wang *et al.* reported that the original structure of ND particles is characterized by a diamond core covered with an amorphous carbon layer, the latter predominantly terminating with electrophilic oxygen species, such as carboxylic acids and their anhydrides. For this reason, it shows a low catalytic activity. Upon increasing the annealing temperature, the  $\text{sp}^2$ -carbon on the ND surface reconstructed from the amorphous form into a well-ordered OLC *via* an intermediate composite BND structure. The latter is characterized by a diamond core covered with a highly defective, curved graphene outer shell. Such a hybrid may act as an appropriate matrix for the formation of ketone-type functional groups and thus exhibits superior catalytic activity.<sup>128</sup>

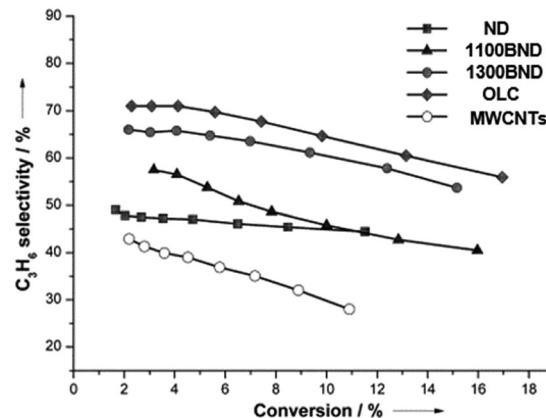


**Fig. 7** Propylene selectivity *versus* propane conversion curves of UNDD catalysts with different annealing temperatures and MWCNTs in the ODH process. Reproduced from ref. 127 with permission Wiley, copyright 2014.

2.2.1.5 *Creation of heteroatom-based active sites in UNDDs.* Since nanocarbon catalysts often may have poor stability at high temperature and low selectivity for olefin products, engineering of the carbon surface to achieve a good overall performance is highly desirable. Heteroatom modification of nanocarbon surfaces is an effective method for such purposes. Recently, doping with P, B and N elements has been demonstrated to be an excellent methodology to enhance product selectivity in the ODH reaction of ethane,<sup>138</sup> propane<sup>139,140</sup> and *n*-butane.<sup>117,141</sup> Recently, BNDs modified with phosphate were applied as an active and selective catalyst for the ODH of propane.<sup>129</sup> Phosphate groups efficiently inhibit the dissociative adsorption of O<sub>2</sub> and improve the catalyst stability, while simultaneously promoting the amount of selective oxygen species. The phosphate addition thus results in an enhanced selectivity. This promotion effect originates from the formation of a covalent C–O–P bond on the modified BND surface. The observed excellent activity could compete with state-of-the-art metal oxide catalysts, with the advantage of no carbon deposition or catalyst deactivation during the reaction.<sup>142</sup>

Borate modification on BND surfaces was used to demonstrate the roles of heteroatoms in catalytic propane ODH.<sup>130</sup> Differently from phosphate doping, borate modification resulted in a volcano-type trend of propene selectivity upon increasing the loading of borate. At a low loading (<15 wt%), the B species mainly interacted with the defects of BNDs by forming an O–H bond. This interaction suppresses the formation of electrophilic oxygen species, thus leading to an increased propene selectivity. However, for a higher boron amount, the formation of tetrahedral coordinated boron leads to a significant blockage of the active carbonyl groups. It is worth noting that these results indicate new mechanisms of interaction between the heteroatoms and the carbon surface, and the related influence on the catalytic behaviour, different from those usually considered in analysing the effect of doping nanocarbons with heteroatoms. These new mechanisms of interaction are specifically enhanced in NDs and related materials, due to their structural and surface characteristics.

the higher productivities, avoidance of solvents and typically less-costly downstream separation procedures, liquid-phase reactions (in the presence of a solid catalyst) offer the advantages of avoiding vaporization costs, and typically better control of selectivity in complex reactions.<sup>153,154</sup> They are thus preferable not only for organic syntheses, but also for many reactions in the area of biomass transformation.<sup>153–155</sup>

Later, a new hybrid structure consisting of a ND-decorated porous  $\beta$ -SiC foam matrix was shown to have an EB dehydrogenation activity ten times higher than that of a commercial K-Fe catalyst and 3.8 times higher than that of pure ND powder. High stability was also observed for at least 100 h, due to the open porosity of the catalyst, which efficiently prevents coke deposition during the reaction.<sup>144</sup>

The surface hydrophilicity/phobicity of BNDs and OLCs is slightly different from that of NDs and BNDs and OLCs show better dispersibility in organic media. It is certain that a variety of the surface groups of UNDDs or dopant-modified UNDDs (*e.g.*, N and B) are capable of providing the underlying access to achieve effective interfacial contact between the substrate and catalyst itself in the liquid-phase reactions. Up to now, UNDDs and dopant-modified UNDDs have been proved as effective heterogeneous catalysts in many important liquid-phase reactions. Some typical liquid-phase reactions of industrial relevance are reviewed in this section.

**2.2.2 Liquid-phase reactions.** While current industrial processes occur in large part under gas-phase conditions, due to



Fig. 8 (a) Sketch for the production of UNDDs and related materials. (b) The possible evolution pathways of different nitrogen species during the preparation process of nitrogen-modified UNDDs (two hexatomic rings as ideal starting model structures in different pathways). Reproduced from ref. 156 with permission from American Chemical Society, copyright 2014.

formation of various N species. Therefore, a high content of nitrogen can be achieved by varying the surface oxygen concentration of the starting BND material. The selective oxidation of benzylic alcohols serves as a probe reaction to evaluate the catalytic performance of the N-BND catalysts (3 examples of reactions with different substituents, see Fig. 9a). The highest yield of benzaldehyde on the N-BND catalysts could reach 18.6%, which is twice higher than that of the pristine BND catalyst. This is attributed to the nitrogen-doping modification. It appears that the bonding behaviour between the nitrogen species with lone-pair electron properties and the free radicals derived from the oxidant may be responsible for the higher reactivity.

Epoxides are important intermediates for fine chemicals like perfumes, drugs, epoxy resins, sweeteners, *etc.* Current research on olefin epoxidation generally relies on the use of metal-based catalysts, such as Au/TS-1.<sup>157,158</sup> Depending on the calcination temperature, nitrogen-doped OLC (N-OLC) catalysts can be synthesized under an ammonia atmosphere (Fig. 8a, pathway II) and the highest nitrogen content could reach 3.95 at%.<sup>159</sup> The N-OLC exhibits superior activity compared to pristine OLC, N-graphene, N-CNTs, Au/TS-1 and Co-OMS-2 in styrene epoxidation (Fig. 9b).<sup>160,161</sup> It was suggested that the graphitic nitrogen species play an important role rather than defects and oxygen species in the epoxidation reaction. In fact, graphitic nitrogen does not directly participate in the activation of styrene, but instead it changes the electronic structure of the adjacent carbon atoms, making them active for the generation of reactive oxygen species such as peroxides.<sup>162</sup> When TBHP (*t*-BuOOH) is used as the oxidant, the adjacent carbon atom to the graphitic nitrogen in N-OLC (Cat) could undergo a one-electron oxidation to form Cat-OH species. Subsequently, the Cat-OH species is converted into intermediate species A (Cat-OO<sup>•</sup>Bu), which is

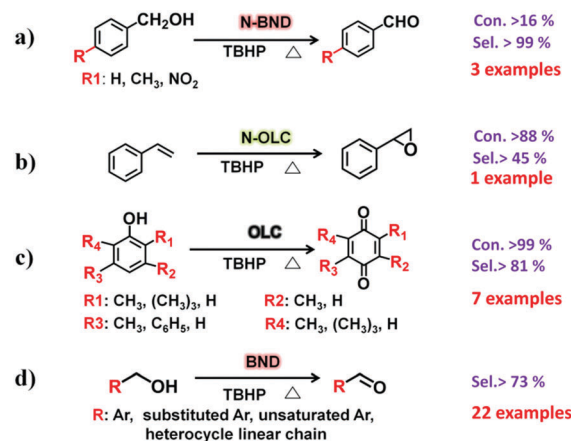


Fig. 9 Schematic illustration for typical liquid-phase oxidation reactions over UNDDs and modified UNDDs.

favourable for triggering the breakup of the double olefinic bond of styrene and the formation of a transition state, B. The latter species finally complete the whole ring-closure process of the epoxide product (Fig. 10). Although the roles of nitrogen species are confirmed, a synergistic effect between the oxygen and nitrogen species over the N-BNDs and N-OLCs in the selected catalytic reactions has not been studied.

**2.2.2.2 Aromatic organic molecules as models.** Nanocarbon materials can be considered as carbon atoms grouped into layers of fused aromatic rings, and containing different types of oxygenated groups (Fig. 11a). Therefore, aromatic organic molecules with specific oxygen functional groups (Fig. 11b) represent model systems having a similar carbon network



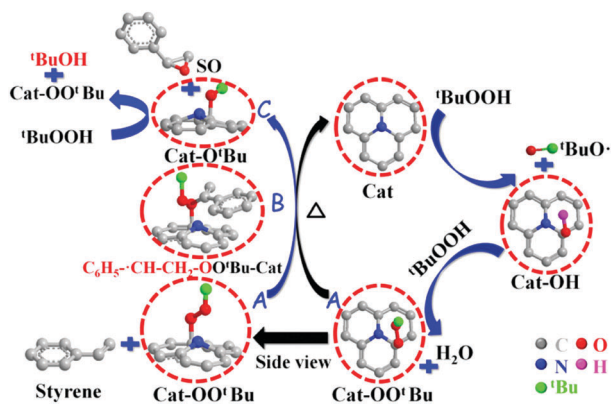


Fig. 10 The proposed mechanistic pathways for epoxidation on N-OLC. Reproduced from ref. 159 with permission from Royal Society of Chemistry, copyright 2014.

structure, surface properties and a tuneable electronic conjugated  $\pi$  system (by extending the benzene unit). They thus mimic the intrinsic structures of oxidized carbon catalysts and allow identifying specific oxygen active components, such as C=O functional groups.

Organic molecules with designated edge configurations (Fig. 11b) can also be used to simulate the armchair and zigzag edge structures of carbocatalysts and to probe the roles of defects in catalysis. This approach can thus provide valuable information for studying the nature of active centers in carbocatalysts and their behaviour in between organocatalysis and solid catalysis.

Recently, Lin and co-workers demonstrated that pristine OLC (Fig. 8a, pathway IV) exhibits outstanding catalytic performance in the selective oxidation of mono-, di- and tri-substituted phenols (7 examples for substrates with different substituents, see Fig. 9c) to the corresponding *p*-benzoquinones. The pristine OLC shows better efficiency than reference systems such as metal-based catalysts (*e.g.*, Ti-HMS, Ti-Si) and industrial catalysts (*e.g.*, 40%  $\text{H}_2\text{SO}_4$ ,  $\text{CuCl}_2/\text{MgCl}_2$ ).<sup>163</sup> The 99.0% conversion for phenols and 81.5–92.5% selectivity for the corresponding benzoquinones can be achieved with OLC under milder reaction conditions.

The authors used different molecules as model catalysts to exclude the roles of oxygen species in the reaction and found



Fig. 11 (a) Surface structure of carbon materials with typical oxygen species and edge defects. (b) Structures of different aromatic organic molecules with single oxygen groups (*e.g.*, C=O, C-OH, C-O-C, -COOH) and designed defect configurations (*e.g.*, armchair and zigzag).

that the edge zigzag configuration assists the reaction by stabilizing the intermediate phenoxy radicals. The catalytic behaviour of OLC was better than those of other carbon materials, such as AC, graphite, graphene, *etc.* More recently,  $\text{sp}^3/\text{sp}^2$ -hybridized BNDs as a potential green catalyst have been shown to exhibit excellent chemoselectivity and cycling stability for the selective oxidation of complex primary alcohols to their corresponding aldehydes (22 examples, Fig. 9d). The observed activity results are comparable to those of conventional Pt/C and Ru/C catalysts for certain substrates under solvent-free conditions. Using the same method of using aromatic model compounds as references, the zigzag edges of surface  $\text{sp}^2$  carbon planes on the BNDs were shown to play a catalytic role in the reaction.<sup>164</sup>

Therefore, aromatic organic molecules with a larger conjugated system and tuneable edge configuration represent a valuable model to understand the nature of carbocatalysts and to develop new applications.

**2.2.2.3 Advanced oxidation processes (AOPs).** A variety of organic compounds was recently detected in industrial and municipal wastewater. Some of these compounds cause serious problems in biological treatment systems due to their resistance to biodegradation. Consequently, finding alternative treatment technologies to mineralize or totally transform refractory molecules into degradable products is a matter of great concern. Among them, advanced oxidation processes (AOPs) have been demonstrated as powerful techniques to produce highly reactive oxygen species which could effectively degrade toxic organic pollutants into harmless products.<sup>165</sup> Transition metal-based materials have been employed as the most effective catalysts for activation of some common oxidants, such as peroxydisulfate (PDS), hydrogen peroxide ( $\text{H}_2\text{O}_2$ ) and ozone ( $\text{O}_3$ ) to form sulfate radicals ( $\text{SO}_4^{\bullet-}$ ), hydroxyl radicals ( $^{\bullet}\text{OH}$ ), and/or superoxide radicals ( $\text{O}_2^{\bullet-}$ ) with higher redox potentials to achieve rapid decomposition of a wide range of contaminants.<sup>166</sup> Metal-free carbon materials represent alternative valuable and less toxic alternatives to catalyze these reactions. They avoid secondary contamination (*e.g.* metal leaching) relative to the use of transition metal-containing catalysts.

Phenol is a model molecule and organic pollutant itself, widely present in industrial wastewater, typically used to test the behaviour in AOP reactions. In 2016, Duan and co-workers showed that different carbon materials including GO, GR, MWCNTs, BNDs and mesoporous carbon as catalysts exhibit excellent catalytic activity for phenol removal in the presence of PMS.<sup>167</sup> Among these nanocarbons, BNDs were found to show better performances. Later, BNDs were shown to promote free radical pathways, with BNDs being able to activate PMS to produce both  $\text{SO}_4^{\bullet-}$  and  $^{\bullet}\text{OH}$ , the latter species being highly active in phenol degradation.<sup>168</sup> The activity is higher than those of typical metal oxide particles, such as  $\text{Fe}_2\text{O}_3$ ,  $\text{Fe}_3\text{O}_4$ ,  $\text{Co}_3\text{O}_4$ ,  $\text{Ga}_2\text{O}_3$  and  $\text{CuO}$ . The unique  $\text{sp}^2/\text{sp}^3$ -hybridized interfaces of BNDs are capable of inducing electron transport from the ND core to the shell surface, enhancing the O-O breakup efficiency in PMS.<sup>168</sup>



Lee *et al.* proposed instead a non-radical oxidation pathway, based on PDS activation and phenol removal *via* electron transfer from phenol to PDS.<sup>169</sup> BNDs only facilitate the electron transfer and reactant adsorption. Lee *et al.* indicated that radical intermediates such as  $\text{SO}_4^{\bullet-}$  and  $\bullet\text{OH}$  are not involved in this persulfate-driven oxidation of phenol.<sup>169</sup>

More recently, a series of BNDs with different graphitized degrees (annealed at different temperatures) were investigated by Duan *et al.* (Fig. 12a).<sup>170</sup> The number of graphitic shells of BNDs, which depends on the annealing treatment, determines the activation pathway of PMS. The radical quenching tests (using MeOH as a radical scavenger, Fig. 12b) suggest that the higher graphitic degree on 1100 BND gives rise to a greater proportion of the non-radical oxidation pathway. This indication is supported by the weaker intensity of the ESR of 1100 BND (Fig. 12c). On increasing the number of graphitic shells, the phenol removal mechanism transforms from a radical-dominated oxidation (for the 900 BND catalyst) to a non-radical-dominated pathway (for the 1100 BND catalyst, see Fig. 12d).

Theoretical calculations indicate that the diamond core would excite electrons to the graphitic shell of one-layer graphene/diamond *via* strong covalent bonds, giving rise to a denser electron population of the carbon sphere, which would promote the charge migration to PMS to generate  $\text{SO}_4^{\bullet-}$ . However, it is difficult for electrons to go through multiple shells in a three-layer graphene/diamond model (*e.g.* 1100 BND), leading to a greater adsorption energy of PMS on the outermost layer of the 1100 BND to form a surface-activated complex for non-radical oxidation (Fig. 12e). Besides, edge defects imply a non-radical pathway for the PMS activation, with quinone groups located at the boundaries having a crucial role in cleaving PMS (by weakening the O–O bond) to produce  $\text{SO}_4^{\bullet-}$ .

A N-BND catalyst with melamine as a nitrogen precursor was proposed with the role of nitrogen in enhancing the activation

of PMS to produce  $\text{SO}_4^{\bullet-}$  and  $\bullet\text{OH}$  associated with the creation of positively charged carbon domains.<sup>171</sup>

**2.2.2.4 Reduction reactions.** Traditionally, the chemoselective hydrogenation of nitro groups to amines is carried out using various transition metal or precious metal catalysts.<sup>172,173</sup>

Lin and co-workers reported for the first time that boron-doped OLC (B-OLC, Fig. 8, pathway III) shows excellent catalytic activity and stability in the nitroarene reduction reaction with  $\text{N}_2\text{H}_4$  (20 examples of substrates with different substituents).<sup>174</sup> The highest yield rate for aniline was reported to be  $593 \mu\text{mol m}^{-2} \text{h}^{-1}$ . The lattice  $\text{BC}_3$  species was suggested to play a positive role in improving the catalytic performance. Compared with the B atom, the C atom has a larger electronegativity. It can be expected that the B atom having an electron-deficient nature in the lattice is the positively charged site.  $\text{N}_2\text{H}_4$  as a strong electron-donating reagent may be adsorbed on the site of lattice B, forming a weak B–H bond together with the activation of H atoms, and thus stabilizing the hydrogen intermediate products and avoiding the fast loss of hydrogen as  $\text{H}_2$ . Once nitroarene substrates are added into the reaction system, the O atoms of the nitro group would abstract the activated H atoms from  $\text{N}_2\text{H}_4$ , leading finally to the high selectivity for desired products and achieving the efficient utilization of  $\text{N}_2\text{H}_4$ .

Importantly, an inverse relationship between the work function and the catalytic performance of UNDDs in the nitroarene reduction reaction was recently proposed.<sup>89</sup> The lower work functions of UNDDs probably induced by their high curvatures inevitably endow them with a higher surface energy that may be beneficial to improve the catalytic activity.

Additionally, Zhang *et al.* developed a novel method to efficiently produce aniline by electrochemically assisted reduction of nitrobenzene using a NDD material as the cathode electrocatalyst.<sup>175</sup> The dominant reduction pathway on the NDD electrode involves the conversion of nitrobenzene to aniline *via* phenylhydroxylamine.

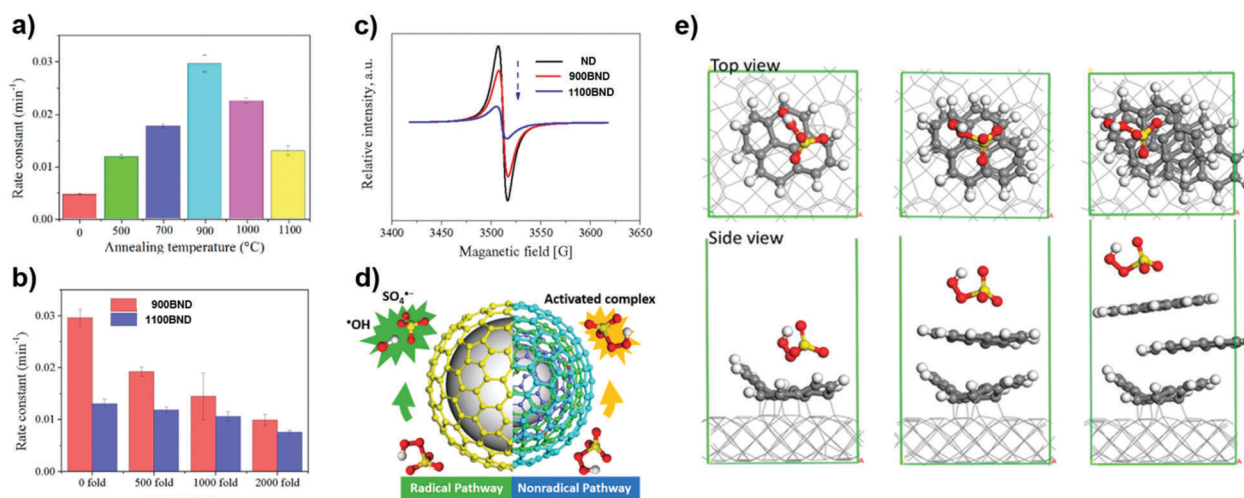


Fig. 12 (a) Influence of different annealing temperatures on phenol removal. (b) Quenching effect of phenol removal on BNDs with different graphitic degrees. (c) ESR spectra of UNDDs. (d) Illustrations of radical and non-radical oxidations on UNDDs. (e) Theoretical modulation of BNDs with different graphitic layers, reprinted from ref. 170 with permission from Elsevier, copyright 2018.









Fig. 14 (a) ORR polarization curves and (b) the calculated  $J_k$  (kinetic current density) values of various catalysts recorded at  $-0.30$  and  $-0.35$  V, in O<sub>2</sub>-saturated 0.1 M KOH, reproduced from ref. 180 with permission from American Chemical Society, copyright 2014. (c) ORR polarization curves and (d) mass activities of N-OLC and Pt/C catalysts recorded at 0.8 V, in O<sub>2</sub>-saturated 0.1 M HClO<sub>4</sub>, reprinted from ref. 192 with permission from Royal Society of Chemistry, copyright 2016.

catalytic performance may be attributed to the synergistic effect among graphitic N, pyrrolic N and pyridinic N.

Using laser irradiation of ND colloidal dispersion in various solvents, OLCs were prepared. These materials were then treated with NH<sub>3</sub> and H<sub>2</sub>S to synthesize N- or S-doped OLC (N-OLC or S-OLC), respectively.<sup>184</sup> The presence of the heteroatoms improves the catalytic performance. The electron transfer values for the N-OLC and S-OLC were calculated to be constant (3.8 and 3.3, respectively) over a potential range from  $-0.3$  V to  $-0.8$  V. The authors proposed that S might enrich electron or spin density in adjacent carbon atoms and promote ORR activity. The pyrrolic N structure can increase the electron delocalization because of their high electron-withdrawing ability and ensure the four-electron pathway of the ORR. Interestingly, this viewpoint was different from most of the previously reported indications on the active sites of nitrogen-doped carbon materials (generally associated with pyridine or graphitic N species).<sup>31,185,186</sup> More recently, N-OLC was also confirmed to be an efficient and robust electrocatalyst in the ORR.<sup>187</sup>

Due to the difference in electronegativity and the number of valence electrons between carbon and boron atoms, the incorporation of boron atoms into the lattice carbon network theoretically should play a positive role in enhancing the ORR activity with respect to boron species located at the edge of the carbon network. A class of B-OLCs (Fig. 8, pathway III) with high substitutional boron shows high ORR stability and tolerance for methanol.<sup>188</sup> The correlation between the catalytic performance and the electronic structures of doped catalysts was analysed in detail by UPS measurements. The results indicate that the presence of boron atoms is capable of lowering the work function, shifting the valence band edge and improving the density of states of the OLCs. All of these aspects

are expected to play a crucial role in enhancing the catalytic performance. Recently, a hot filament assisted CVD technology has been utilized to obtain porous boron doped diamonds (BDDs) deposited on a nickel foam substrate. A certain amount of boron atoms can be successfully incorporated into the crystal lattice of diamonds and thus influence the catalytic activity.<sup>189</sup>

Additionally, the incorporation of P into OLC was studied in an effort to promote the catalytic performance in the ORR and to adjust the electronic structure of the carbon network.<sup>190</sup> Different phosphorus chemical states were investigated, and C–O–P bonds were proven to be responsible for the enhanced activity.

The physicochemical properties of UNDDs, and behaviour in the ORR, can also be tuned by forming nanocomposites with other nanocarbons. Liu *et al.* applied N,B co-doped graphitic carbons as shell materials to fabricate ND/N,B co-doped graphitic carbon with a core/shell structure.<sup>191</sup> This method utilizes effectively the chemical stability of the sp<sup>3</sup> carbon in NDs for electrocatalysis, allowing the use of NDs with low conductivity.

Interestingly, the most recent works on the ORR involve alkaline media and the possible application in acidic media has rarely been described. A nitrogen doped diamond@carbon-onion hybrid nanostructure (actually, it is also NOLC) was found to show a remarkably enhanced ORR performance, although the mass activity calculated from the Tafel plot for the NOLC catalyst was only about 40% of that of reference Pt/C (Fig. 14c and d). The authors proposed that the hybrid structure of the graphitized OLC, with N-doped edges at the shell and residual sp<sup>3</sup>-hybridized ND structure at the core, conceived a synergistic effect with a considerably enhanced ORR.<sup>192</sup> This work sheds light on the possibility of metal-free carbons as promising catalysts in the ORR with acidic media.

Up to now, UNDDs or doped UNDDs have been proven potential competitors to Pt-based catalysts for the ORR in alkaline media or acidic media, even if performances have to be further improved. Although few studies on the understanding of the O<sub>2</sub> activation mechanism and the formation of intermediates were carried out on nanodiamond-type electrocatalysts, the roles of different species or edge structures in UNDDs or dopant-modified UNDDs have been in general still limitedly studied. In order to understand better the intrinsic active sites and relevant reaction processes, it is useful to review briefly below some fundamental attempts to unravel ORR mechanisms on other nanocarbon catalysts. These insights could provide indications on how to translate the findings to UNDDs and derived ORR electrocatalysts, even if it is out of the scope here to discuss in depth the ORR mechanism on carbon materials.

In 2009, Dai and co-workers reported that N-doped carbon nanotubes (NCNTs) with a vertically aligned structure can act as a metal-free electrocatalyst.<sup>193</sup> Such NCNT materials exhibited much better electrocatalytic activity, long-term operational stability, and tolerance to the crossover effect than the Pt–C/GC catalyst. The enhanced catalytic performance was attributed to nitrogen dopant atoms neighboring to carbon atoms, resulting in a substantially higher positive charge density (left-hand side of Fig. 15).



Meanwhile, the O<sub>2</sub> activation process during the ORR was also proposed. The presence of nitrogen induces charge delocalization and thus changes the chemisorption mode of O<sub>2</sub> from the common end-on adsorption (Pauling model) on the CNT surface (top right of Fig. 15) to a side-on adsorption (Yeager model) onto the NCNT catalysts (top right of Fig. 15). This modality of adsorption allows effectively weakening the O–O bonding and facilitates the ORR. Later, Hu *et al.* found that pristine CNTs are not favorable for realizing O<sub>2</sub> adsorption.<sup>194</sup> In contrast, the adsorption of O<sub>2</sub> on the NCNTs is exothermic in nature and involves electron transfer to O<sub>2</sub> related to the promotion of the energy level of the highest-occupied molecular orbital (HOMO) and the simultaneous reduction of the gap between the HOMO and the lowest-unoccupied molecular orbital (LUMO) after nitrogen doping. The authors suggested that the electron configuration of O<sub>2</sub> on the NCNTs was similar to that of O<sub>2</sub>-species.<sup>194</sup>

Actually, due to the lack of specific doping of selected N species, different types of N species coexist in nitrogen-doped nanocarbons. At least three nitrogen forms were considered (pyrrolic, pyridinic and graphitic N) to be possible active sites. The O<sub>2</sub> dissociation behavior on different N species or different N active sites is still unclear. Additionally, the local structure of N in the carbon network is still an open question.

The energy barriers of the oxygen molecule dissociation on graphitic N, nitrogen-substituted Stone–Wales defect and pyridinic N were studied by Yang's group.<sup>195</sup> When one nitrogen atom was incorporated into the SWCNT lattice, the oxygen adsorption energy did not obviously change compared with pure SWCNTs at the initial stage. The highest energy barrier of the O<sub>2</sub> dissociation decreased to 0.86 eV from 1.61 eV of SWCNTs (Fig. 16a and b). Upon increasing the concentration of nitrogen and tuning the arrangement modes of nitrogen (*meta*-, *para*-positions) in the carbon lattice, the corresponding energy barriers of the O<sub>2</sub> dissociation were reduced to 0.42 and 0.69 eV (Fig. 16c and d). The carbon atom adjacent to both nitrogen atoms had a more positive charge. The O–O bond length became 1.37 Å, longer than the previous two cases (a and b).

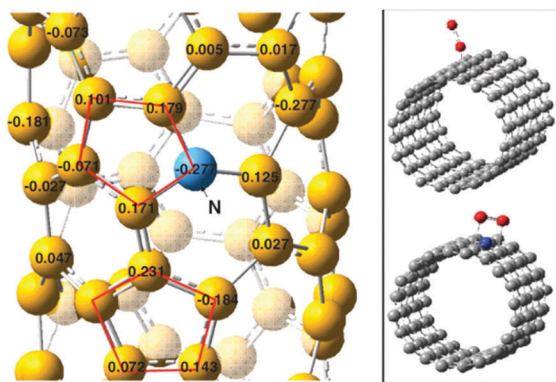


Fig. 15 Calculated charge density distribution for the NCNTs and schematic representations of possible adsorption modes of an oxygen molecule at the CNTs (top) and NCNTs (bottom), reprinted from ref. 193 with permission from Science, copyright 2009.

After introducing one nitrogen atom to substitute in the Stone–Wales defect (a common defect), in the final dissociated state, one oxygen atom would adsorb on a carbon top site and the other oxygen atom would break the C–C bond, forming a C–O–C ether linkage (Fig. 16e). The energy barrier of the O<sub>2</sub> dissociation was 0.49 eV. In the case of O<sub>2</sub> dissociation on pyridinic N (Fig. 16f), the corresponding energy barrier was 1.28 eV, also lower than that for pristine SWCNTs.

Therefore, the energy barriers can be reduced efficiently by common types of nitrogen doping. Graphitic N and Stone–Wales defect nitrogen were found to be more efficient in decreasing the energy barrier with respect to pyridinic N, due to their lower dissociation barrier. We will further discuss the activation of a single Stone–Wales defect nitrogen for O<sub>2</sub> later.

The preparation of doped nanocarbons with single nitrogen species is the best way to determine directly the actual roles of each nitrogen species in the ORR, but it is still challenging. Recently, Guo *et al.* utilized HOPG model catalysts with well-defined  $\pi$  conjugation and well-controlled doping of N species to identify the real active sites.<sup>69</sup> The measured concentration ratios of graphitic (grap) N and pyridinic (pyri) N in grap-HOPG and pyri-HOPG are up to 82% and 95%, respectively (Fig. 17a). ORR results show that the pyri-HOPG model catalyst exhibits high activity at high voltages. The pyri-HOPG sample with lower

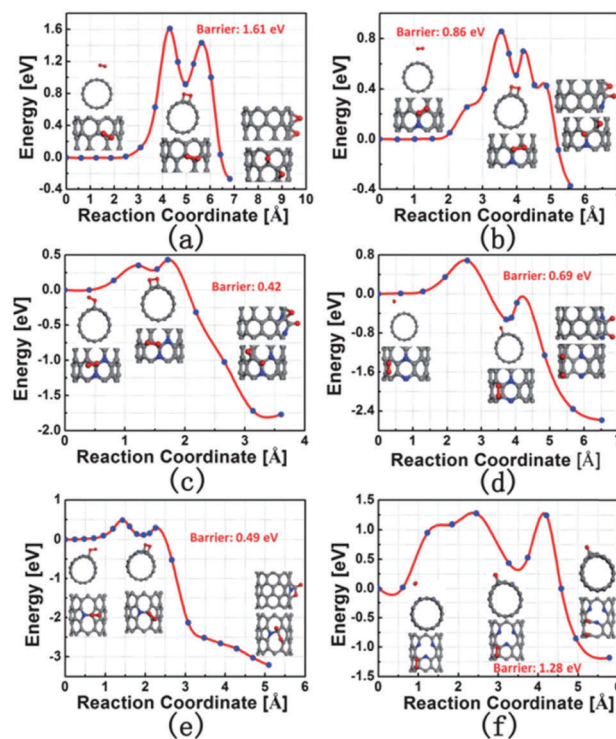


Fig. 16 Optimization energy pathways of oxygen molecule dissociation on (a) pure (8,0) SWCNTs, (b) one nitrogen atom substituted (8,0) SWCNTs, (c) two *meta* nitrogen atom substituted (8,0) SWCNTs, (d) two *para* nitrogen atom substituted (8,0) SWCNTs, (e) one nitrogen atom substituted (8,0) SWCNTs with a Stone–Wales defect, and (f) (8,0) SWCNTs with pyridine-like nitrogen atoms. Gray dots, blue dots and red dots represent carbon, nitrogen and oxygen atoms, respectively, reprinted from ref. 195 with permission from Royal Society of Chemistry, copyright 2011.

N concentration (N: 0.60 at%) is much more active than the grap-HOPG sample with higher N concentration (N: 0.73 at%). The results indicate that pyridinic N rather than graphitic N reduces the ORR overpotential and creates the active site (Fig. 17b).

Using the TPD-CO<sub>2</sub> methodology, it is found that the Lewis base site (*i.e.* the carbon atom neighboring the pyridinic N dopant atom) is the active site for the ORR. Oxygen molecules can be adsorbed on these Lewis base sites to achieve the initial step of the ORR followed by protonation of the adsorbed O<sub>2</sub> (A–B steps of Fig. 17c). Two pathways are then possible: (i) the first is the common 4e<sup>−</sup> mechanism occurring at a single site; and (ii) the second is a 2e<sup>−</sup> mechanism. In the former mechanism, two H<sup>+</sup> attack the two oxygen atoms, leading to the breakage of the O–OH bond (C step) and the formation of OH species (D step). In the last E step, the additional H<sup>+</sup> would react with the adsorbed OH to form H<sub>2</sub>O. In the case of the 2e<sup>−</sup> pathway, intermediate H<sub>2</sub>O<sub>2</sub> is generated by reaction of the adsorbed OOH species with another H<sup>+</sup> (F step). Subsequently, H<sub>2</sub>O<sub>2</sub> is readsorbed and reduced by two H<sup>+</sup> to form H<sub>2</sub>O.

Several experimental results in combination with theoretical calculations have pointed out that the enhanced activity of nitrogen-doped carbon materials is related to modification in the charge density at C-atoms lying near to N dopants. This effect induces Lewis acidity on these carbon atoms due to both the electronic effect and local deformation of aromaticity.

For B-doping, the vacant 2p<sub>z</sub> orbitals of B conjugates with the carbon  $\pi$  system to extract the electrons were reported. These electrons would become quite active due to the low electronegativity of B, and thus O<sub>2</sub> molecules would be adsorbed on the positively charged B sites to achieve the ORR process.<sup>196</sup>

B,N-Codoping is a possible route to optimize metal-free nanocarbon ORR electrocatalysts. However, theoretical calculations indicate that when N with extra electrons interacts with B atoms having a vacant orbital, mutual neutralization may occur. In contrast, separated B and N doping can turn CNTs into excellent ORR electrocatalysts.<sup>197</sup>

Not only is the role of heteroatoms still controversial, but the role of edges in nanocarbons for ORR behavior is also still a matter of debate. Shen and co-workers suggested that edge carbon atoms are more active than the basal-plane ones for the ORR. In their ORR experiment, an air-saturated electrolyte solution droplet (diameter *ca.* 15  $\mu$ m) was deposited at a specified position either on the edge or on the basal plane of HOPG. It was found that the ORR on the edge occurs at a more positive onset potential and with a higher current density than that on the basal plane of HOPG.<sup>198</sup> In addition, this group applied an Ar plasma etching method to prepare a series of edge-rich nanocarbon materials. After plasma treatment, the I<sub>D</sub>/I<sub>G</sub> value is obviously improved from 1.16 to 1.51. The onset potential and the reduction peak potential of edge-rich nanocarbons significantly shift to positive values with respect to the pristine nanocarbon electrode, demonstrating the positive role of edges in the ORR.<sup>199</sup>

To date, carbon-based or doped carbon-based materials have been extensively investigated as efficient metal-free electrocatalysts for the ORR. Various single-, dual- or multi-doped systems including N, B, P and S catalysts have been made. A lot of theoretical calculations have been used to identify active sites and to explain the ORR mechanism. However, the exact interpretation of the mechanism and active site of the ORR on nanocarbons is still rife with controversy. Consequently, it is even more difficult to derive unique conclusions in the case of nanocarbons with intrinsically higher degrees of complexity, as the nanodiamond and related materials discussed here. More importantly, the possible rate-determining step (RDS) has been rarely studied using experimental methods so far. The roles of electron transfer (ET) and proton coupled electron transfer (PCET) processes in the ORR should be highlighted. One of them unavoidably involves the RDS depending on catalysts used. Furthermore, the possible application of carbon-based materials in acidic media should be further demonstrated.

**2.3.2 CO<sub>2</sub> reduction reaction (CRR).** Due to the excessive consumption of fossil fuels, the content of CO<sub>2</sub> in the atmosphere

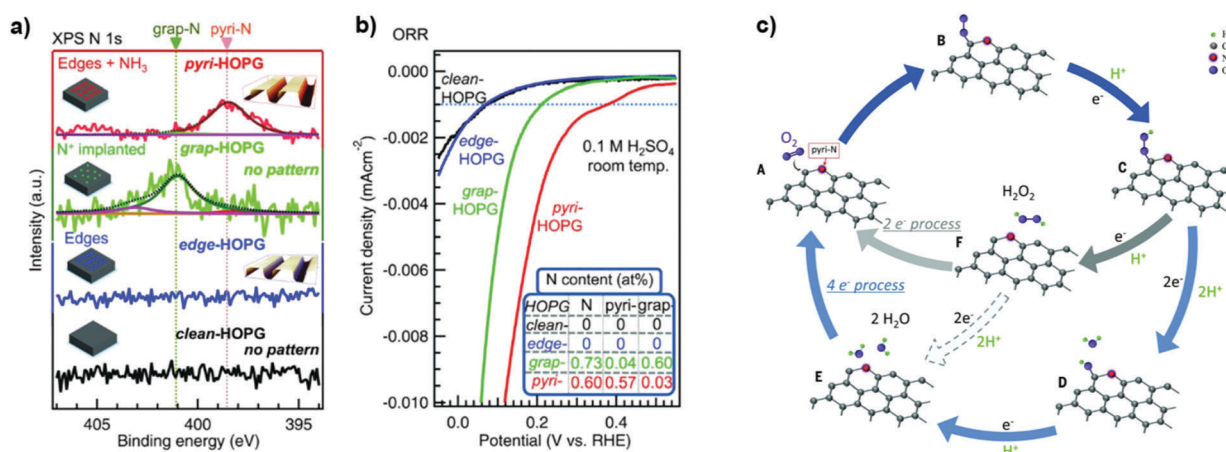


Fig. 17 (a) N 1s XPS spectra of various catalysts. (b) ORR results for various catalysts with high concentrations of pyridinic N or graphitic N species. The inset shows the nitrogen contents of the catalysts. (c) Schematic pathway for the oxygen reduction reaction on nitrogen-doped carbon materials, reprinted from ref. 69 with permission from Science, copyright 2016.





and oceans has dramatically increased. A series of problems associated with resources, the environment and climate have been highlighted. Achieving effective recycling and utilization of CO<sub>2</sub> is thus highly necessary, from both ecological and economical standpoints.<sup>200–202</sup> The electrochemical reduction of CO<sub>2</sub> (namely the CRR) could provide an attractive solution to these issues, in which CO<sub>2</sub> is converted into useful fuels and utilized as a chemical feedstock.<sup>17,202,203</sup> This CRR possesses some intrinsic advantages of (i) operation under ambient conditions; (ii) electrochemical processes controlled by modulating externally applied potentials and electrolytes; (iii) cyclic utilization of electrolytes to significantly reduce the overall chemical consumption; and (iv) composability in the electrocatalytic reaction system.

In most of the studies on heterogeneous catalysis made using metal electrodes (*e.g.* Cu), the main products obtained through the CRR have been CO or formic acid.<sup>204</sup> Some other high value-added products, including formaldehyde, methanol, and methane, have also been achieved using semiconductor or other metal electrodes under atmospheric or high-pressure conditions. These products generally involve direct transfer of electrons to a CO<sub>2</sub> molecule, which requires a high reduction overpotential. Therefore, it means that the hydrogen evolution reaction is a competitive process. In fact, the protons and electrons for CO<sub>2</sub> reduction should derive from the electrolysis of H<sub>2</sub>O on the anodic part of the electrochemical cell, but the produced H<sup>+</sup>/e<sup>−</sup> in the water oxidation (anodic) step may recombine to form H<sub>2</sub> (on the cathodic side) rather than being used for CO<sub>2</sub> reduction and hydrogenation. This side reaction to H<sub>2</sub> reduced the faradaic selectivity in CO<sub>2</sub> conversion.

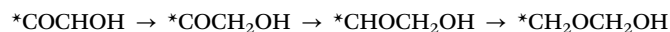
It is of note that often high faradaic selectivities have been reported, but at very low current densities, *i.e.* very low productivities. Often the faradaic efficiencies were not achieved under the same conditions where reaction rates in the target product of CO<sub>2</sub> reduction are reported. Using a microwave plasma assisted CVD method, a BDD electrode producing a high yield of formaldehyde (C1 product) in the CRR was obtained.<sup>205</sup> The highest faradaic efficiency for formaldehyde reached 74% at −1.7 V *vs.* Ag/Ag<sup>+</sup> at room temperature and atmospheric pressure even if formic acid was also observed with the best faradaic efficiency of 15% at −1.5 V *vs.* Ag/Ag<sup>+</sup> in a MeOH electrolyte. When seawater is applied as electrolyte, formaldehyde could be still formed with a faradaic efficiency of 36%. In comparison with the MeOH electrolyte, the lower faradaic efficiency is attributed to the narrow potential window in water and the influence of the inorganic and organic impurities in seawater. The authors proposed that the high faradaic efficiency was attributed to the sp<sup>3</sup>-carbons in the BDDs.

Liu *et al.* synthesized a NDD/Si rod array (NDD/Si RA), *i.e.* analogous to that shown in Fig. 13, observing high efficiency in the CRR to formate (C1) and acetate (C2) products.<sup>206</sup> It was found that CO<sub>2</sub> would be preferentially and rapidly converted to acetate over formate with an onset potential of −0.36 V (*vs.* RHE) in 0.5 M NaHCO<sub>3</sub> solution. The behavior overcomes the common limitation of low selectivity for C2 products. Upon increasing the concentration of nitrogen from 0.93% to 2.12%,

the production rates for acetate and formate increase significantly. Faradic efficiencies of about 91–92% for formate and acetate can be achieved at −0.8 to −1.0 V. The superior performance was attributed to the high overpotential for hydrogen evolution and to the presence of N-sp<sup>3</sup>C active sites (*e.g.* sp<sup>3</sup> type C atoms near to a N doping atom). The main pathway for the CRR is indicated as follows:<sup>206</sup>



Recently, they further found that a BNND material is an efficient and stable electrode for the CRR to produce directly ethanol with a high faradaic efficiency of 93.2% at 1.0 V (*vs.* RHE).<sup>207</sup> The faradaic efficiency for CH<sub>3</sub>CH<sub>2</sub>OH is maintained around 93% after a 16 run test, which reflects the high durability of the BNND material for the CRR (Fig. 18a and b). Using the DFT method (Fig. 18c), a series of possible intermediate products are proposed. The high selectivity of CH<sub>3</sub>CH<sub>2</sub>OH may be due to the easy occurrence of the C–C coupling reaction (namely \*CO → \*COCO) on the BNND material. The free energy of the whole CH<sub>3</sub>CH<sub>2</sub>OH formation process is negative, meaning that reducing CO<sub>2</sub> to CH<sub>3</sub>CH<sub>2</sub>OH is thermodynamically favorable on the BNND material. The presence of B may improve CO<sub>2</sub> capture by bonding with one O atom of absorbed CO<sub>2</sub> (\*CO<sub>2</sub>). Moreover, the B atom also plays an important role in facilitating the following reactions:



by forming a B–O bond (Fig. 18d). The role of N may promote \*H transfer in the elementary reactions involving hydrogenation by reducing the energy barrier of the reactions. A possible pathway for the CRR involves the following sequence of reactions:



N- or B-(co)-doped UNDDs have shown promising behaviors in obtaining high-value added chemicals (C1 and C2) in the CRR. Similar to the ORR, the recent development with doped UNDDs as electrocatalysts in the CRR is still in its infancy. The roles of various N species or boron species have not been investigated. Ma *et al.* summarized the present status and future challenge of metal-free carbon materials in the CRR.<sup>208</sup>

Some examples of the catalytic behavior of nanocarbons other than UNDDs will be introduced here for a better understanding of the reaction mechanism in the CRR, although a detailed discussion of carbon materials different from UNDDs is out of scope here.

A range of 3D nitrogen-doped graphene nanoribbon networks (N-GRW) with tunable N species were designed to reveal the site-dependent CRR activity/selectivity reported by Liu *et al.*<sup>209</sup> The N-GRW catalyst exhibits a high CO faradaic efficiency of 87.6% at a mild overpotential of 0.49 V. A linear regression can only be produced between current density and the concentration of pyridinic N. After using post-hydrogen treatment to reduce



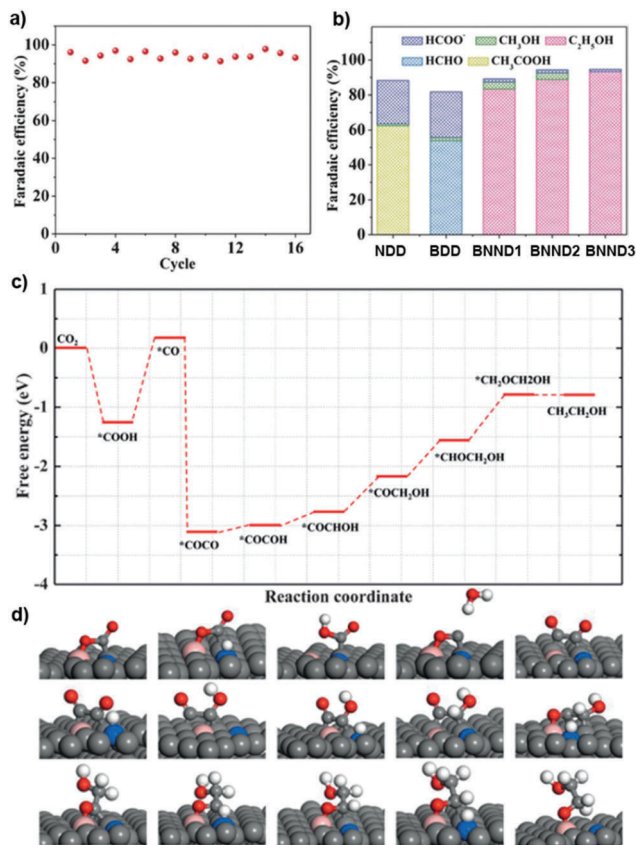


Fig. 18 (a) Faradaic efficiencies for CH<sub>3</sub>CH<sub>2</sub>OH in 16 consecutive CRR runs on BNND3 at 1.0 V. (b) Faradaic efficiencies for the CRR on different catalysts at 1.0 V. (c) Free energy diagrams for the CRR on BBNDs. (d) Energetically favorable structures for elementary steps of the CRR on BBNDs. Gray dots, pink dots, blue dots, red dots and white dots represent C, B, N, O and H atoms, respectively, reprinted from ref. 207 with permission from Wiley, copyright 2017.

the content of oxidized N and graphitic N species, the change in the CRR activity along with pyridinic N content can also be fitted into a good linear relation (Fig. 19a), suggesting that pyridinic N could be the active site. Phosphoric acid treatment was further used to reduce selectively the pyridinic N of the N-GRW by adsorption. The activity of the soaked N-GRW is lower than that of the original N-GRW (Fig. 19c), further indicating that the CRR activity should be determined by the pyridinic N sites. The plausible reaction mechanism mainly involves two intermediates (\*COOH and \*CO). Compared with pyrrolic N, graphitic N and oxidized N have higher  $\Delta G$  values. Pyridinic N has a lower  $\Delta G$  value of 0.33 eV, implying that it is beneficial for the transformation of CO<sub>2</sub> to \*COOH and further to \*CO (Fig. 19d).

The origin of activity in N-doped nanocarbons for the CRR has also been investigated by Xu *et al.*<sup>210</sup> These electrocatalysts show excellent performances, with about 90% current efficiency for CO formation and stability over 60 hours. The N-doping was realized using a specific surface methodology, based first on the creation of O-functionalities and then their reaction with a positively charged polyelectrolyte (poly(diallyldimethyl-ammonium chloride), PDAA) as the N source. Depending on PDAA loading and

the temperature of annealing, different N species are formed. It is possible to quantify their amount (for example, by XPS) and then correlate the amount of the different species with the onset potential for the CRR. A good correlation with the amount of quaternary N species was observed, while no relationship was found with the other N species. The role of these quaternary N doping atoms, as indicated by DFT calculations, is to stabilize the carbon dioxide radical anion (\*CO<sub>2</sub><sup>-</sup>), formed by one-electron transfer, thereby lowering the initial reduction barrier and improving the intrinsic activity.

For the CRR, the presence of many pathways of transformation with analogous energy and the presence of the side reaction of hydrogen evolution significantly influence the yield of the target products. However, at the same time, literature data show that selectivity could be achieved beyond what can be expected from a thermodynamic analysis of the possible reaction pathways. This indicates that it is thus the electrocatalysis, rather than just electrochemistry, which determines the possibility of achieving high performances.<sup>203</sup> On the other hand, literature data are often not presented in the right way to understand the potential applicability, which is the faradaic efficiency at high current densities per geometrical area of the electrode.

Note also that it is often not clearly excluded that the products observed in the CRR do not derive from the nano-carbon itself, either from organic contaminations or from the direct reduction of the more reactive carbon species. At the same time, reconstruction of the carbon species may occur during the electrocatalytic reaction, as noted before for dehydrogenation reactions. A more extended use of *in situ/operando* methods is necessary, but using specific model electrocatalysts, which can unravel the complex electrocatalytic chemistry present in CRR systems. Compared with the ORR, the CRR system is more complicated (more H<sup>+</sup> and e<sup>-</sup> transfers, depending on products) and thus more intense investigation on the nature of the active sites and the reaction mechanism is necessary. Studies on interfacial effects including CO<sub>2</sub> adsorption, diffusion, activation and product formation, and desorption processes on the catalyst remain challenging.

At the same time, however, it is necessary to parallel these fundamental studies with others with practical character, where relevant data for exploitability of the results (faradaic efficiency at high current densities, productivity to target products per geometrical electrode surface, stability over extended periods) are presented. In addition, often the results in the literature are obtained in electrocatalytic reactors, which are not relevant for industrial use (the use of large electrolyte volumes, batch cells, for example) or not taking into account important aspects such as product recovery, cell fluidodynamic and current homogeneous distribution in larger cells, formation of gas caps, *etc.*<sup>203</sup>

**2.3.3 Other electrocatalytic reactions.** In addition to the ORR and CRR, other electrochemical applications have been explored in the past few years. For example, Liu *et al.* further showed the excellent performance of a NDD/Si rod-array in the electro-reductive debromination of polybrominated diphenyl ethers.<sup>211</sup> The kinetic constants of such nanomaterials were



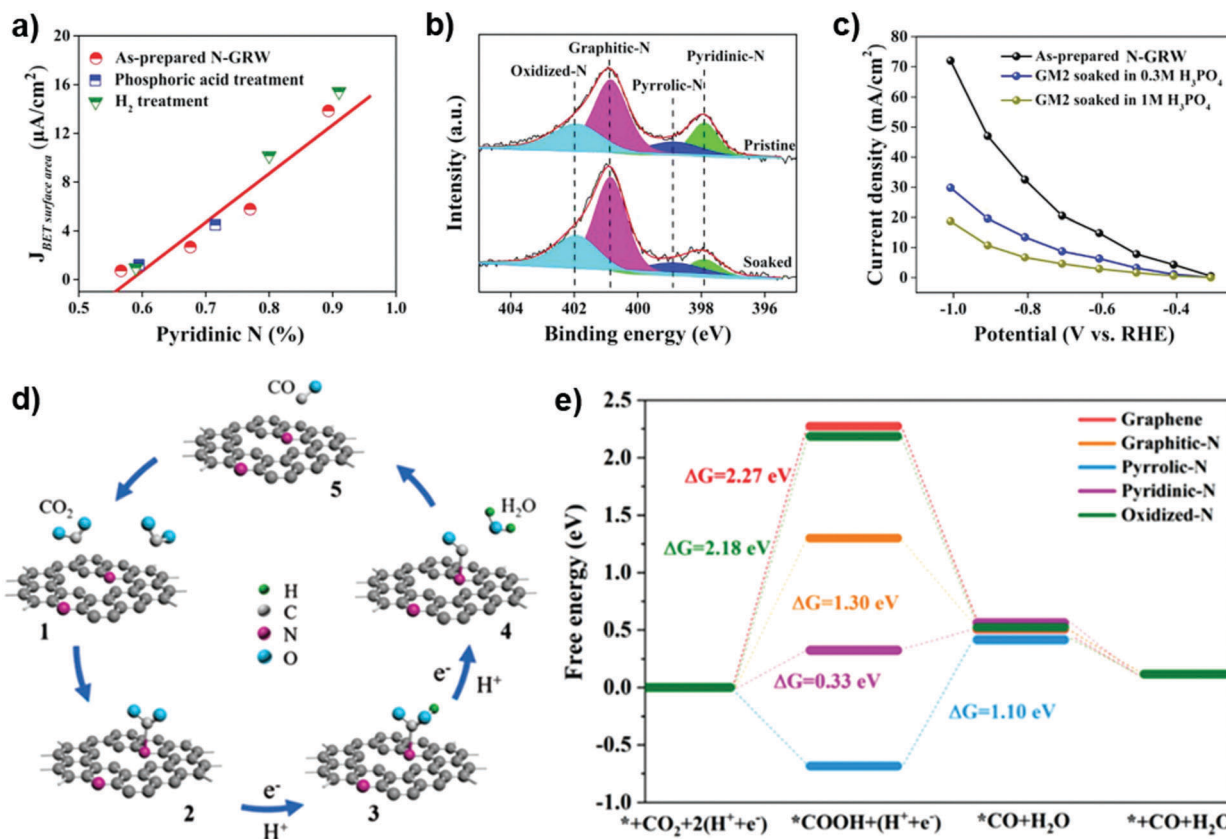


Fig. 19 (a) The relationship between the CO current density and the pyridinic N content in various N-GRW catalysts at 0.5 V (vs. RHE). (b) N 1s XPS spectra of N-GRW before and after being soaked in 1 M  $\text{H}_3\text{PO}_4$  aqueous solution. (c) The multipotential curves of the N-GRW, N-GRW soaked in  $\text{H}_3\text{PO}_4$  aqueous solution with different concentrations for half an hour. ORR results for model catalysts. (d) Illustration of the CRR processes on N-GRW catalysts. (e) Free energy diagram of the CRR on various N species, reprinted from ref. 209 with permission from Wiley, copyright 2018.

much higher than those of pure ND, graphite, Pt wafer and Pd film electrodes under the same conditions. It was suggested that the improved activity was due to the low hydrogen evolution potential, N-doping induced active sites, enlarged surface area and facile charge transport. Moreover, an electrochemical oxidation of nitrite to nitrate on a ND-based electrode was reported by Chen and co-workers.<sup>212</sup> N-OLC and B-OLC have also been demonstrated to be efficient anodes for long-life Li- $\text{O}_2$  and Na- $\text{O}_2$  batteries, respectively.<sup>213,214</sup>

## 2.4 Photocatalytic reactions

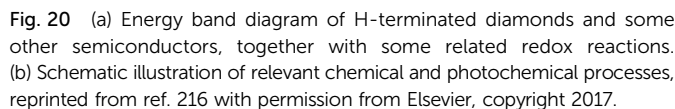
In general, photocatalysis is the catalysis of a photochemical reaction on a solid surface.<sup>215</sup> Photocatalysis includes two main branches: one involves energy-related photocatalysis (e.g. water splitting,  $\text{CO}_2$  reduction,  $\text{CH}_4$  activation), and the other is environmentally-related photocatalysis (e.g. organic pollutant degradation). To date, photocatalysis has been considered as a promising sustainable technology, because it allows the direct use of solar light, although with the main limitation of low reaction rates, making commercial photocatalytic processes to be used to a limited extent. Current studies on photocatalysis are largely using oxide or derived materials (oxynitrides, for example). Their development is mainly focused on three crucial aspects: (i) improving the full visible-light harvesting and use,

(ii) enhancing the charge separation of the photogenerated species, and (iii) increasing the efficiency in the use of the photogenerated charges for the chemical reactions, particularly by adding co-catalytic functionalities. Carbon-based materials have been limitedly considered as possible photocatalysts.

Due to the specific electron structure and fast charge carrier combination, metal-free carbon materials (except  $\text{C}_3\text{N}_4$ ) are not suitable options for photocatalysts in principle. However, the great flexibility of modification of nanocarbons, with the possibility of creating semiconducting zones as commented on later, nanodots and other photoactive functionalities, combined with the presence of a chemically active surface with unique properties induced by doping/defect engineering as well as by the presence of edges provides new possibilities for photocatalysis still largely unexplored.

Fig. 20a compares the energy band diagram of H-terminated diamonds with those of some other typical semiconductors, such as GaN,  $\text{TiO}_2$ , CdS and SiC. It is evident that the H-terminated NDs present rather interesting possibilities for overcoming the theoretical energy barrier to initiate the one-electron reduction of  $\text{CO}_2$ , the reduction of  $\text{H}^+$  to form the solvated  $\text{H}^\bullet$ , or to form the solvated  $\text{e}^-$  (aq) even if the band gap of the ND is up to 5.47 eV, which lies in the insulator range. It was shown that H-terminated NDs dispersed in 18.2 M $\Omega$  cm





More recently, Tripathi and co-workers proposed that a water soluble OLC exhibits better catalytic activity for the degradation of methylene blue (MB, a typical organic pollutant dye) than that of pristine OLC under visible light irradiation.<sup>218</sup>

There are thus limited studies on the use of NDs and derived materials as photocatalysts, but the preliminary indications suggest that this is an area of potentially larger interest. There is, in general, increasing interest in the use of nanocarbon materials as photocatalysts or components in photoanodes.

Although some excellent achievements have been realized using UNDD or doped UNDD catalysts, there is in general still a lack of in-depth mechanistic studies on the reaction and on UNDDs to identify the specific peculiarity of this novel class of carbocatalysts. From the previous discussion, it was evident that the charge density on specific C atoms or C-C bonds induced by the curvature of the surface graphene layer, associated with the presence of a hybrid  $sp^2/sp^3$  configuration and/or doping with heteroatoms, plays an important role, eventually in synergy with other functional groups (*e.g.*, C=O). The amount of functional groups in general is higher than those in other nanocarbon materials, as well as the presence of defects. The highly defective surface could:

- facilitate absorption of the reactants, stabilize intermediates or enhance the desorption rate of the products;
- generate the active sites, which may be associated, for example, with the zigzag edge configuration that was proof to play a key role in some liquid phase reactions;
- lead to the *in situ* formation of active sites (*e.g.*, C=O) by dissociating oxidants/reductants during the reaction.

All these characteristics are associated with the peculiar electronic structure of these highly defective materials and the additional effect of the local curvature in the graphene-like plane. These structural characteristics make possible also an *in situ* reconstruction during the catalytic reaction, with generation of new active sites induced by these transformations.

The introduction of heteroatoms (*e.g.* N) in UNDD catalysts improves largely the catalytic activity. Taking the ORR and CRR as examples, several common N species including pyridinic N, graphitic N, pyrrolic N or N-sp<sup>3</sup>C species were speculated to be active sites, but their exact roles as well as defect species, the evolution of the related species and surface microstructure changes (*e.g.*, arrangement) during the electrochemical reaction are largely not understood.

For instance, the C=O group can alter the electronic distribution of the surrounding carbon atoms on the UNDD surfaces and facilitate the adsorption/desorption of catalytic reaction intermediates, and thus may affect the electrocatalytic activity. Moreover, the roles of carbon corrosion and carbon restructuring, particularly in electrochemical applications, should be taken into account. The reaction pathways and nature of the active sites involved in the formation of different

products (C1, C2) during the CRR should be explored in detail. There is, in general, a lack of mechanistic studies on these carbocatalysts for their knowledge-based development.

## 2.6 Nano-structuring the catalytic sites

This term defines the design of the optimal nano-scale spatial arrangement of multiple functional centers, which are necessary in a catalytic site for complex multistep catalytic reactions. One of the research directions for a future sustainable chemical production is the process intensification realized through a reduction in the number of steps.<sup>37,154</sup> Realizing multifunctional catalysts able to make one-pot multistep (cascade) reactions, requiring different catalytic functionalities, is thus one of the areas of development for catalysis in general. In addition, it is also necessary to optimize the diffusion of the reactants (and the retrodiffusion of the products) as well as eventually define an optimal path of diffusion in the solid in order to have the target sequence of active centers and reactions.

This is one of the actual frontiers of research in catalysis and nanocarbons, particularly NDs and related materials, have several of the requirements to develop these types of materials. However, it will be necessary to develop novel procedures of synthesis and post-modifications to develop the aimed characteristics and catalytic functionalities, together with the methodologies to determine the optimal 3D-configurations for multifunctional active centers. This requires combining advanced modelling and specific methodologies for determination of the nature of active sites in carbons at the nano-scale level. It will also be necessary to assemble specific carbon nano-units to create 3D-like structures with specific porosity characteristics, allowing both mass and heat transfer limitations to be avoided. This controlled nano-morphology, from the nano- to macro-scale, is necessary to limit the rates of the parallel or consecutive side reactions, which is sometimes even more critical than in “classical” catalysts, due to the presence of a charged surface and charged species deriving from electron transfer.

This concept of nano-engineering is present in the literature, but a solid and more systematic use in the development of nanocarbon catalysts is still lacking. The starting point is to design an efficient and robust mechanism to synthesize and assemble nano-components, based on an improved understanding in the nature of the active sites in nanocarbons. This is a concept going beyond that of hierarchically organized materials, which consider essentially aspects related to mass-transfer of reactants and products. It will also include the possibility of the development of nano-hybrid architectures, based on the combination of nanocarbons and other (such as oxide nanoparticles) elements.

Notwithstanding research on nanocarbons has largely focused on the synthesis procedures, as emerged also from the previous sections, further efforts in this direction are necessary.

## 3. From NDs to catalysis by nanocarbons

The previous section showed how novel types of nanocarbons with respect to the common classes of materials (such as

graphene, CNTs and fullerene families, *i.e.* the most used and discussed in recent reviews) provide valuable opportunities to improve the performances and to extend the use of metal-free nanocarbons for new applications. Both these aspects are largely associated with the possibility of going beyond the concept of doping with heteroatoms, the most common aspect analysed in the literature. Although clearly this is an important aspect, the results show that the doping with heteroatoms creates a localized charge density on C atoms or C–C bonds, and these centers represent the active sites by themselves or acting in cooperation with the functionalities introduced by the heteroatoms.

This is an area largely at the beginning of understanding, requiring also the development of specific methodologies of analysis. From this perspective, however, it is evident that there is a wider range of possibilities for changing the surface properties of nanocarbons than just by doping/co-doping:

- curvature and creation of strains in C–C bonds;
- creation of hybrid  $sp^2/sp^3$  systems (eventually with stabilized  $sp^1$  centers as well);
- design of tailored defects and vacancies.

These elements integrate with the functionalities generated by doping to form a powerful platform of possibilities for tailoring the surface properties, and for this reason making nanocarbons a unique, potentially disruptive class of catalysts. The combination of all these tailoring methods may be called defect engineering in nanocarbons.<sup>20,29</sup>

Many aspects have been already discussed in the previous section. Here we analyse how some of the above elements have been considered in the analysis of the catalytic behaviour of other nanocarbons, although in our opinion there is a lack of a more holistic and integrated analysis of their role in understanding the catalytic behaviour of nanocarbons.

The previous section has remarked on how understanding the catalytic chemistry of NDs and related materials requires considering the synergy between catalytic functionalities created by (i) doping, (ii) nanostructure effects (curvature associated with nanostructures or other elements), (iii) edge effects and (iv) creation of reactive carbon atoms or bonds due to electron density localization. The same concept is valid to understand catalysis by nanocarbons in general.

We will present some aspects in the following sections to support this generalized concept to understand catalysis by nanocarbons, in particular in association with the last aspect often underestimated. However, it is out of the scope of a systematic analysis, being limited to evidence that this synergy is not just a peculiar property of NDs and related materials, but a general and crucial aspect to understand nanocarbon reactivity.

### 3.1 Defect-related catalytic reactivity

Nanocarbons contain the highest number of defects with respect to other types of catalysts such as oxides.<sup>219</sup> This is related to the higher structural flexibility in nanocarbons, particularly NDs and related materials, to minimize energy due to defects through local instead of extended restructuring.



For example, an isolated pentagon transforms a SWCNT into a sharp cone, and a heptagon converts it to a horn.<sup>220</sup> This also explains why hybrid nanocarbons such as the nanodiamond family described in the previous section contain typically a higher number of defects. A common defect in nanocarbons is a pair of pentagon–heptagon (5/7). Their presence causes changes in the chirality of SWCNTs.<sup>220</sup> The formation energy of a 5/7 defect site in SWCNTs ranges between 2 and 4 eV and thus is quite low. The chirality in the growth of SWCNTs is determined from defect healing.<sup>221</sup> A generalized model for the growth of defective MWCNTs was proposed by Hembram and Rao.<sup>222</sup> Defects such as pentagons, heptagons, vacancies, or dopants are found to modify drastically the electronic properties of these nanosystems.<sup>223</sup>

The presence of defects and vacancies in nanocarbon materials is thus well established, but their role in the catalytic properties is often underestimated, in part due to the difficult characterization. Most of the studies on carbocatalysis do not analyze the presence and role of these sites.

Nevertheless, there are indications that defects and vacancies play both a direct role, inducing the formation of active sites (dangling bonds, which have characteristics different from those present on edge sites, and may easily have a cooperative effect), and an indirect role, by (i) inducing change in the local charge density at nearby C atoms or C–C bonds, (ii) creating semiconducting states, as discussed later, and (iii) hosting metal ions or atoms. DFT calculations indicate that defects in graphene sheets can reach a concentration of up to about 1%. This effect creates also localized energy levels near to the Fermi level. Consequently, an effect on the local charge and catalytic reactivity is observed.<sup>224</sup> Defects in graphene sheets thus generate three types of modifications:

- create reactive sites;
- change the electronic state and adsorption characteristics;
- change the conduction characteristics, which are clearly relevant not only in electrocatalysis, but also for catalysis itself, due to the possibility of delocalizing electrons (in redox reactions), generating radical species and even transporting the heat of reaction (thus reducing, for example, local increases in temperature – electron and heat transfer in carbon materials depend on similar parameters).

It was reported that defects in CNTs determine their degree of functionalization and types of functional groups generated, with a consequent change in the behavior in biomass conversion.<sup>225</sup> The production of reactive oxygen species during irradiation and thus the photocatalytic behavior in CNTs depend on the type of defect.<sup>226</sup> Highly defective CNTs show high photocatalytic activity.<sup>227</sup> A base and acid washing of graphene creates a defective material showing high activity in the oxidative coupling of amines to imines.<sup>228</sup> Hole defects in the conjugated domain were indicated as the active sites in this reaction, or alternatively the carboxylic acid terminating edges in the hole defect. Characterization of these materials by ESR indicates a relationship between the catalytic behavior and the localized spins in the edges related to the *p*-electron system. These sites with unpaired electrons activate molecular oxygen by a sequence of electron transport and reduction to superoxide radicals.

Mechanically induced defects in CNTs greatly modify their characteristics and the reactivity in derived Pt/CNT electrocatalysts used as anodes in PEM-type fuel cells.<sup>229</sup> It is worth noting that it was demonstrated how these defects induce many modifications in these electrocatalysts:

- change the dispersion of Pt particles;
- improve the tolerance of the catalyst to CO poisoning, due to the carbon functional groups in close proximity to Pt particles and which catalyze the reactivation of Pt sites poisoned by CO;
- affect the electronic conductivity of CNTs;
- modify the hydrophilic character, with a consequent influence on the three-phase boundary and the protonic transport to the active metal particles.

Therefore, the effect of creation of defects cannot be correlated with specific parameters typically used to analyze the electrocatalytic behavior, such as the geometrical surface area of Pt particles or the electrochemical active surface area determined by cyclic voltammetry (CV) tests.

Zhong *et al.* showed the direct role of edge sites and defects in determining the catalytic behavior of NDs in the decomposition of methane.<sup>131</sup> By quantifying the amount of defect sites through SIMS, *i.e.* by analyzing the signal of  $C_2H_2^-$  (acetylene-like fragment – it is a fingerprint of hydrogenated defects) with respect to  $C_2H^-$  and  $C_2^-$  signals (fingerprint for aromatic C–H groups and aromatic/graphitic carbon, respectively), it was possible to estimate the concentration of defect sites in ND samples annealed at different temperatures. The initial rate of methane decomposition was observed to depend linearly on the number of  $-CH=CH-$  defective sites (Fig. 21).

DFT studies give indications on the reaction pathways and mechanisms. The rate-limiting step is the initial C–H bond cleavage in methane having an energy of about 2.47 eV. The transition state interacts with one of the carbon atoms in the vacancy, producing a  $-CH_3$  group which further loses the hydrogen at another vacancy site. The process then further continues at the carbon vacancy site, as shown in Fig. 22.



Fig. 21 Initial rate of reaction in  $CH_4$  decomposition at 850 °C versus the  $C_2H_2^-/C_2^-$  ratio in SIMS spectra of ND samples, which were annealed in the 900–2000 °C temperature range. Adapted from ref. 131 with permission from Royal Society of Chemistry, copyright 2014.





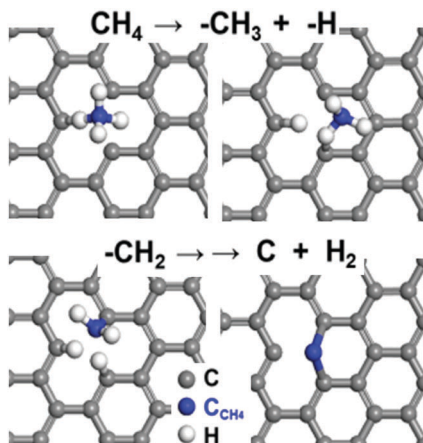


Fig. 22 Mechanism of reaction in methane decomposition at defect sites in nanocarbons. Based on indications of ref. 131 with permission from Royal Society of Chemistry, copyright 2015.

There are thus some examples in the literature on defect-related catalytic reactivity in nanocarbons, but in general attention on these aspects is limited, due to the difficulty in analyzing and characterizing the defects and vacancies in nanocarbons, their high dependence on the specific preparation conditions and the strong correlation with other characteristics of nanocarbons and thus the intrinsic difficulty in enucleating the specific aspects.

The introduction of defects in nanocarbons influences, among others, the (i) surface reactivity, (ii) mobility of adspecies, (iii) hydrophilicity, and (iv) electron conductivity. Thus, a proper determination of the relation to the catalytic behavior requires investigating all these aspects and their relative contribution to the catalytic performances.<sup>139</sup>

### 3.2 Modification in the charge density at carbon atoms

As briefly commented on above, the presence of defects, curvature and heteroatoms induce changes in the charge density at localized C atoms or C–C bonds. This results in the creation of potential active sites, whose role has been scarcely investigated up to now. Sidik *et al.* indicated that the reduction of O<sub>2</sub> (ORR) is facilitated on the in-plane carbon atom adjacent to the substitutional N atom.<sup>230</sup> Kim *et al.* also indicated that oxygen activation occurs on a C atom adjacent to a pyridinic-N at the edge of a graphene nanoribbon.<sup>231</sup> The proposed catalytic cycle involves a ring-opening of the cyclic C–N bond which can be restored after the 4e-reduction of the chemisorbed oxygen (Fig. 23). Although also different ORR mechanisms (as discussed in Section 2.3.1) have been proposed,<sup>31,232</sup> the one given in Fig. 23 shows both the role of defects sites/edges and the direct participation in the reaction mechanism of C atoms having nearby heteroatoms.

Stone–Wales defects are a common type of nanocarbon defect. They are characterized by the presence of two five-membered rings and two seven-membered rings, substituting four adjacent six-membered rings of a pyrene-like region. The C–C bond bridging two of the adjacent rings rotates, creating a reactive C–C bond bridging the two five-membered rings. When nearby heteroatoms are present, this may create a different charge

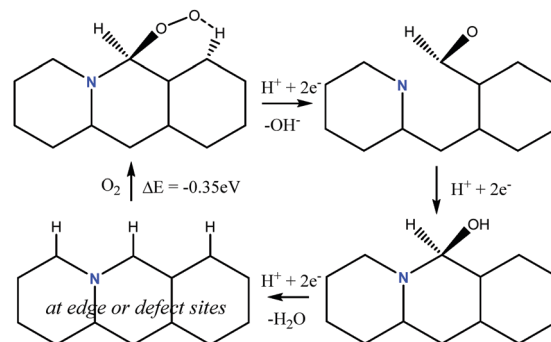


Fig. 23 The ORR mechanism suggested for N-doped graphene edges, evidencing how O<sub>2</sub> adsorbs at carbon adjacent to a N-atom. Based on indications of ref. 231 with permission from Royal Society of Chemistry, copyright 2016.



Fig. 24 (a) Model of N<sub>2</sub> activation at Stone–Wales defects with nearby doping N sites (in blue). (b) Model of O<sub>2</sub> activation at reactive C–C sites in Stone–Wales defects on the surfaces of graphene-like materials with specific curvature. Based on the model given in ref. 233 with permission from American Chemical Society, copyright 2014.

density at the carbon atoms in this reactive C–C bond, as illustrated in Fig. 24a, where the numbers at the C atoms indicate the effective charge density. Chai *et al.* indicated that nitrogen pair doped Stone–Wales defect provides a good active site for the ORR, with the activity being tuned by the curvature around the active site.<sup>233</sup> The maximum limiting potential (0.80 V) in the volcano plot for the ORR activity can be estimated, in agreement with experimental indications. Fig. 24b illustrates the proposed reaction mechanism of O<sub>2</sub> activation, which is followed by breaking of the O–O bonds and stabilization of the surface species by the concerted 2H<sup>+</sup>/2e<sup>−</sup> transfer and formation of a C(OH)–C(OH) species, which then desorbs water.

The curvature plays a potential important role in determining the reactivity of C–C bonds, although very limitedly investigated in terms of catalytic reactivity. Sabirov *et al.* showed by DFT that in the fullerene series C<sub>20</sub>–C<sub>76</sub> there is a correlation between the heat of 1,3-dipolar addition reaction and the carbon surface curvatures at reaction sites.<sup>234</sup> Yang *et al.* using the radial deformation of SWNTs caused by the strong interactions with quartz lattice tubes reported that samples with larger degrees of radial deformation show more delocalized partial electrons at certain sidewall sites with high local curvature, suggesting a relationship with their reactivity.<sup>235</sup> By studying using DFT the reactivity of the C<sub>20</sub>–C<sub>80</sub> fullerene series, Anafcheh *et al.* indicated a correlation in various reactions between the H-abstraction from the primary and secondary C–H bonds of hydrocarbons with the curvature degree.<sup>236,237</sup>



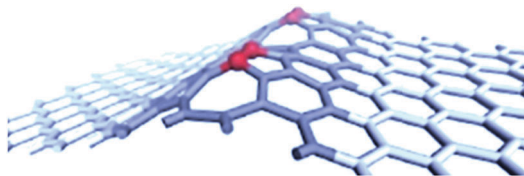


Fig. 25 Visualization of the effect of curvature in creating reactive C–C sites.

There are thus limited data, which indicate the role of the curvature (in graphene or equivalent structures) in creating reactive sites, which is schematically illustrated in Fig. 25, although clearly should be differentiated by irreversible reaction (as often occurs on fullerene materials) and catalytic reaction, in which a mechanism close to the catalytic site should be present.

An example of the role of curvature in influencing the behavior of carbocatalysts is given by the use of OLC-like carbon nanospheres. These materials, showing a high surface area and porosity interesting for catalytic applications, are characterized by a spherical macro shape with relevant structural disorder in the stacking of the graphitic layers together with the presence of small ordered domains.<sup>238</sup> They are active in reactions such as glycerol etherification,<sup>239</sup> and carbon monoxide and methane chlorination.<sup>240</sup> The role of strained C–C bonds related to curvature was well demonstrated for the last case, with differentiation between irreversible and reversible (catalytic) chemisorption.<sup>239</sup> The characterization of these catalysts evidences the presence of strained and highly-strained C–C bonds. The latter were associated with the disordered nano-onion type structure, and react irreversibly with  $\text{Cl}_2$  with the dissociation of the Cl–Cl bond. These sites are analogous to those in fullerenes, where high bending is present and which also react irreversibly with  $\text{Cl}_2$ . The other strained C–C bonds form from the first during thermal annealing nano-ordering. These sites are reactive towards  $\text{Cl}_2$ , but form a reversibly coordinated  $\text{Cl}_2$  molecule. The coordination of CO forms  $\text{COCl}_2$  and that of  $\text{CH}_4$  leads to chlorinated methane products. It was observed that C–C bonds with moderate to weak straining character instead do not or only very weakly coordinate  $\text{Cl}_2$ .

The proposed catalytic mechanism of CO chlorination on these catalysts, after thermal annealing to control the strain character of the C–C bonds, is schematically illustrated in Fig. 26 assuming a fullerene hemisphere as a model of the effective nanostructure.

### 3.3 Creation of semiconducting areas

As discussed above, UNDDs were demonstrated to be a category of promising photocatalysts in water splitting,  $\text{CO}_2$  reduction and organic pollutant degradation. A perhaps unique characteristic of nanocarbon materials is the possibility of creating interesting photocatalytic properties through generation of semiconducting areas with the band gap tunable even within the visible-light region. These aspects, not having counterparts in oxide-based conventional semiconductors, derive from the possibility of local band engineering through a combination of



Fig. 26 Catalytic mechanism of CO chlorination on a fullerene hemisphere with controlled curvature, as a model for OLC-like carbon nanospheres. Reproduced from ref. 240 with permission from Wiley, copyright 2015.

controlled introduction of defects, doping with heteroatoms and modification of the curvature.<sup>70</sup>

To understand these possibilities, it is useful to introduce first the electronic characteristics of an ideal graphene structure. The in-plane ordering of hexagonal carbon units, with all C-atoms with  $\text{sp}^2$  hybridization, leads to the formation of  $\pi$ -orbitals below and above the C-plane. The  $\pi$ -electrons can move freely and thus this material has a semi-metal electrical character. When the graphene sheet is rolled up to form a tube (SWCNT), the conduction properties will markedly depend on the diameter of the tube and chirality. While a part (about one third) of the possible conformations of the SWCNT are metallic, the remaining conformations have a semiconductor character, with the band gap being inversely proportional to the diameter. It decreases from about 0.8 to 0.4 eV in passing from 1 to 5 nm tube diameter.

This band gap is too small for photocatalytic applications, but may be modified to have wider band-gap semiconductors by inducing controlled defects.<sup>241</sup> Small rotations of a bond, periodically repeated through the lattice, collapse the Dirac cones at the graphene  $K$  point. The electronic structure of graphene is characterized by bands, which are cones intersecting at the Fermi surface, *e.g.* at the  $K$  points in the Brillouin zone. The band gap is related to the distance between the apex of these cones. Patterned defects can break the graphene sublattice symmetry, creating a band gap. Small area ordering of defects thus generates a local semiconducting area.

Yeh *et al.* showed that N-doped graphene oxide quantum dots could act as visible-light photocatalysts for overall water splitting.<sup>242</sup> They suggested the idea that p- and n-type semiconducting domains form in these nanocarbons. The different domains are associated with different types of doping and defects, as exemplified in Fig. 27. Although this mechanism was not jet proof, Yeh *et al.* indicated that the nanostructure reported in Fig. 27 shows a bandgap of around 2.2 eV, suitable for photocatalysis with visible light. In addition, the p- and n-type domains act as Ohmic spaces, which are p–n junctions allowing an efficient electron–hole separation. Water splitting may occur at the edges of the n- and p-type domains.





Fig. 27 Mechanism<sup>242</sup> suggested for the photocatalytic water splitting on nitrogen-doped graphene. Reproduced from ref. 70 with permission from Elsevier, copyright 2017.

Yeh *et al.* reported for these carbocatalysts (loaded with small amounts of Pt) a quantum efficiency of 12.8% at 420 nm in the photocatalytic  $\text{H}_2$  evolution in aqueous triethanolamine.<sup>243</sup> Even in the presence of a sacrificial agent, the results are promising and superior to those of  $\text{g-C}_3\text{N}_4$  and other Pt-doped conventional photocatalysts.

Although more solid proof is necessary about the presence of these n- and p-type domains and their structures, these indications outline how nanocarbons can have unique properties, characterized by local semiconducting domains in a conductive matrix. There is no equivalent in conventional semiconductors to design advanced photocatalysts based on the possibility of creating nano-sized and tunable n- and p-type domains. In addition, semiconducting nanocarbons differentiate from conventional semiconductors in particular in terms of the following aspects: band structure and pinning at the interface, formation of heterostructures, charge separation, quantum confinements, and charge carrier mobility.

### 3.4 Strains and defects induced by nanocarbon interaction with supported metal nanoparticles

Carbon materials are well-known supports for metal nanoparticles and the development of carbon-oxide nanoparticle hybrids or composites.<sup>58,71,244–249</sup> However, attention is always paid to the reactivity of the supported nanoparticles, although it is well established that the properties largely depend on the specific nature of the nanocarbons, and that the presence of functional groups, doping heteroatoms and defects (although the latter aspect is often not considered) influence largely the catalytic reactivity. Depending on these characteristics, the shape and the reactivity of the supported nanoparticles can be largely influenced.<sup>250–252</sup>

The interaction between the metal nanoparticles depends on both the functional groups in CNTs and the degree of graphitization.<sup>253,254</sup> What is interesting is that a closer inspection by HRTEM of the supported nanoparticles indicates that (i) not



Fig. 28 HRTEM image of a Pd nanoparticle supported over a functionalized CNT. Small arrows indicate new defective areas created at the carbon–nanoparticle interfaces, while large arrows indicate carbon shells wrapping the nanoparticle.

only are the nanoparticles themselves sitting at defect sites, but they also introduce new deformations and defects (indicated by smaller white arrows in Fig. 28), and (ii) also highly defective carbon shells (indicated by large white arrows in Fig. 28) may wrap the nanoparticles during the thermal treatment or catalytic reaction. The effect depends on the type of functionalization and nanostructure of the nanocarbon.

This indicates that the carbon–nanoparticle interaction not only influences the characteristics of the supported nanoparticles, but also changes the feature of the interface itself, with generation of a highly defective carbon region around the nanoparticles, and the possible generation of carbon shells wrapping the nanoparticles. This could stabilize the nanoparticles against the sintering and change their available area, but eventually creating access to a smaller area or crystal faces of the nanoparticles, influencing the activity and selectivity. There are very few data in the literature on these aspects, especially regarding how the catalytic reactivity depends on these aspects. However, it can explain the very large influence of the modification of carbon characteristics and functionalization over the catalytic behavior of the supported nanoparticles.

Another aspect related to the previous observation is that the creation of a highly defective area, or of very thin carbon shells (likely highly defective) wrapping the nanoparticles, creates new carbon-related active sites, as discussed previously. This is an aspect largely not considered in the literature, but some recent evidence indicates that this aspect could be the critical one.

The direct electrocatalytic synthesis of  $\text{NH}_3$  from  $\text{N}_2$  and  $\text{H}_2\text{O}$  could be realized at room temperature and pressure using iron nanoparticles supported over oxygen-functionalized CNTs.<sup>255,256</sup> *Operando* electrocatalytic studies indicate that iron particles transform into  $\text{FeOOH}$  nanoparticles during the reaction,<sup>257</sup> which is important because they may allow realizing a multi-electron transfer of electrons/protons to chemisorbed  $\text{N}_2$ , with a reaction mechanism similar to that present in nitrogenase enzyme.<sup>203</sup>  $\text{N}_2$  activation, however, occurs at carbon sites at the interface with the iron nanoparticles, possibly C atoms with





specific charge density nearlying defects or doping heteroatoms. When a potential of  $-2.0$  eV is applied, a carbon shell wraps the iron nanoparticles, as shown by HRTEM images, leading to an increase of 4–5 times the reaction rate in ammonia formation.

Therefore, although this area is just at the beginning and more in depth studies are required, there are some initial indications that the carbon interface around the nanoparticles could play a direct role in catalysis and electrocatalysis, even in highly challenging reactions such as ammonia direct synthesis.

## 4. Identification and quantification of active sites

A variety of characterization methods are employed to study various active sites (*e.g.* C=O, defects, N species) as well as reaction mechanisms. Among them, some advanced *in situ* XPS and DRIFT technologies are used to reveal the real role of C=O in gas phase reactions. The role of defects is preliminarily investigated by SIMS. Identification and quantification of active sites, however, is still rife with controversy because of the surface complexity of carbon materials. To date, although DFT is the most common way to simulate the intermediates and analyze reaction pathways at a molecular level, but there are various limitations including the use of real reaction conditions (temperature, solvent, *etc.*) and simulation of complex structures with different types of defects, *etc.* It is thus highly desired to develop new technologies to identify and quantify the active sites to understand their role in reaction mechanisms. In this section, we will highlight some promising methods.

### 4.1 Model catalysts

In Section 2.2.2.2, the potential application of aromatic organic molecules as model catalysts in determining active sites was briefly discussed. Although the feasibility of this strategy has been demonstrated in some catalytic reactions involving defects or C=O active sites, more in-depth investigation on other heteroatom species should be emphasized, such as pyridinic N species. It should be noted that aromatic organic molecules with a shorter  $\pi$ -conjugated system (upper part of Fig. 29) might be only appropriate for liquid phase reactions, because of their limited solubility in solvents. With regard to high temperature-driven gas phase

reaction and electrically-driven electrochemical reaction, better thermostability and conductivity for aromatic organic molecules are essential.

By chemical synthesis, a series of polycyclic aromatic hydrocarbon (PAH) organic molecules with single armchair, C=O and pyridinic N configurations and enhanced  $\pi$ -conjugated systems could be prepared (lower part of Fig. 29). We believe that these model catalysts can be used directly in most reactions to experimentally identify real active sites of carbon catalysts or doped carbon catalysts. It can also be expected that designing other PAHs with different B, P or S species is an effective procedure to unravel the specific reactivity of the active sites formed in nanocarbons by doping.

### 4.2 Chemical titration measurements

Although active sites can be identified using model catalysts, the quantification of active sites on carbon catalysts is still challenging because of the detection limit of current common measurements, such as the locality of XPS for catalyst surfaces. Herein a chemical titration method to determine the surface concentration of three kinds of typical oxygen functional groups (C=O, C-OH and COOH) on the surfaces of carbon nanotubes was proposed by Qi *et al.*<sup>258</sup> During the titration process, some chemicals (Fig. 30, PH, BA and BrPE) with the ability to selectively react with different oxygen groups are introduced. Through selective deactivation of these specific oxygen functional groups and the assessment of the catalytic activity of titrated CNTs for EB ODH reactions, the intrinsic active sites (C=O) can be identified and quantified simultaneously. Importantly, the chemical titration measurement method has the potential to be *in situ* operated in some catalytic reactions.

### 4.3 Isotopic labeling measurements

A better understanding of the reaction mechanism requires determining the reaction kinetics of the catalytic process. The common research scope contains the reaction order, reaction rate and activation energy. The use of the kinetic isotope effect (KIE) is an established experimental technique to study chemical reactions involving H, C, O, N and so on.

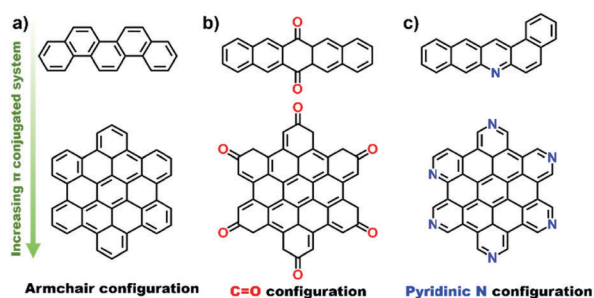


Fig. 29 Polycyclic aromatic hydrocarbon (PAH) organic molecules with single (a) armchair, (b) C=O and (c) pyridinic N configurations as model catalysts.

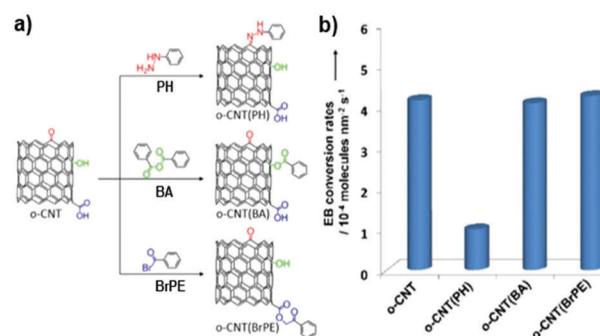


Fig. 30 (a) Schematic drawings of the chemical titration process for oxygen functionalities on oxidized CNTs (o-CNT). (b) EB ODH conversion rates of o-CNT and titrated o-CNT. Adapted from ref. 258 with permission from the Wiley, copyright 2013.



In short, more and more measurements will be developed and promoted as research progresses, such as *in situ/operando* NEXAFS/ESR spectroscopy. Here, we just highlight three kinds of facile methods to gain insight into carbon catalytic essence.

UNDDs offer, in our opinion, distinct characteristics from other types of nanocarbon materials and the scope of this review was to highlight how they offer not only the possibility of developing improved thermal, electro- and photo-catalysts, but also of showing how they open new conceptual perspectives for the design of advanced nanocarbon catalysts.

The key aspects discussed in this review regarded the presence of hybrid  $sp^2/sp^3$  configurations, defect and nano-engineering in the various aspects related to the role of defects and vacancies in the catalytic behaviour, the creation of active sites by modification in the charge density at carbon atoms or C–C bonds, the generation of strained C–C bonds by curvature and other mechanisms, and the formation of semiconducting areas and defect sites at the interface with supported nanoparticles.

We believe that UNDDs represent unique catalytic materials and a unique class of nanocarbons, where these aspects and their synergistic interaction could be demonstrated to have a relevant role in understanding their behaviour and the development of catalysts with improved performances. This is related to their peculiar structural, surface and electronic characteristics. However, they are features relevant in catalysis by all types of nanocarbons. The better understanding of these aspects that we consider often underestimated will lead to new or improved applications. Even if the roles of the single aspects have been reported in the literature, we feel that a more comprehensive picture is missing, so the necessary further step is to exploit the potential disruptive character of these materials.

(1) The abundant surface groups and different basic and acid sites (oxygen species) can serve as a promising platform for rational design of efficient and stable catalytic systems relevant to these different groups.

(3) The exploitation of UNDD-based catalysts requires that they be shaped into industrially usable pellets. It is necessary to develop hierarchically structured materials, which can be used as catalysts or 3D-type electrodes.

(5) It is possible to prepare a class of pristine or heteroatom modified-carbon quantum dots with tuneable properties *via* a facile chemistry dispersion approach, but their use to develop advanced catalysts is still quite limited. Hybrid  $\text{sp}^2/\text{sp}^3$  nanocarbon materials offer new possibilities in this direction, although in UNDDs, for example, achieving a tuneable band gap and controlling the electron characteristics is still a challenge. The development of new practical applications, such as photocatalysts, semiconductor devices, diodes based on nanocarbons and novel photoelectrodes to produce solar fuels,<sup>260</sup> requires understanding the role of defect engineering and the presence of hybrid  $\text{sp}^2/\text{sp}^3$  nanostructures in the rather unique characteristic of creation of mixed semiconductor domains with n/p character. In general, the role of nano-scale design in the photo-activated properties of these materials is a crucial, but still requires large effort and better guidelines on the methodologies and assessment of the results.

(6) Heteroatom co-doping offers interesting possibilities for developing UNDD materials with Lewis acid (*e.g.*, B) and Lewis base sites (*e.g.*, N, P, F), which will provide important opportunities for reactions such as borylation, hydrosilylation, hydrogenation, cycloaddition of CO<sub>2</sub>, and C–H activation. These materials also offer new opportunities to design catalysts with frustrated Lewis pair character. In general, there are unique possibilities for creating multifunctional catalysts able to realize in one-pot multistage reactions.

In conclusion, UNDD materials have been demonstrated to exhibit richer surface chemistry properties and peculiar electronic structures in comparison to other carbon materials. Some recent achievements have shown their outstanding and stable performance in many catalytic reactions, making them alternative options to metal or metal-based catalysts.

The interest in nanocarbon materials as novel catalysts has been largely increasing recently (as an example, the number of entries in SciFinder for the term “metal-free carbon catalysis” was 59 in the 2000–2005 period and over thousand in the



2012–2017 period). Various reviews have been published on nanocarbons, as commented on in the Introduction. However, most of them were focused on describing the synthesis and application of families of materials such as graphene and CNTs, and their modification by doping, with the discussion of the catalytic behaviour related mainly to the functional groups deriving from the introduction of heteroatoms.

UNDDs have been studied in less detail with respect to other types of nanocarbons, such as graphene, CNTs and derived materials. They were also never specifically reviewed. We thus hope that this review has opened new possibilities for a better understanding of these catalysts. At the same time, these results are creating new clues for a better design of the nanocarbon catalyst family.

It should be remarked that systematic studies on the relationship between the nature of these active sites in UNDDs and their catalytic reactivity are still limited. Intensified effort is necessary in advanced *in situ/operando* techniques to understand the catalytic mechanism, but integrated with direct advanced catalytic methodologies, such as combination of surface functional group titration, isotopic labelling methods and high-energy X-ray imaging technology. Attention should be paid also to the effect induced in surface charge or electron density localization on reactive C atoms or C–C bonds. A proper identification and quantification of the active sites is necessary. There are novel methodologies available, as summarized in Section 4, although with still limited utilization.

Compared with conventional carbon materials (*e.g.*, CNTs, graphene, AC), the superior catalytic activities of UNDDs derive from their unique microstructure, electronic structure and surface properties, such as tuneable  $sp^2/sp^3$  ratios upon temperature changes, local curvature effects, stabilization of defects and vacancy sites, low  $\pi$  and  $\sigma$  electronic binding energies, enhanced DOS, low work functions, controllable surface modifications and bulk doping. However, the respective role of  $sp^2$  and  $sp^3$ -bonded carbon and the in-depth mechanism of heteroatoms in the catalytic process need to be further explored. Specific methodologies to single-out the specific contributions also have to be developed. The interaction between active domains and substrates on the surfaces of catalysts, the solvent effect and the kinetics in liquid-phase reactions should be investigated for a better understanding. To date, preparing model carbon catalysts with applicable  $\pi$  conjugated structures (*e.g.*, seven benzene units or above) and designated single species (*e.g.*, only C=O, pyridinic N, zigzag or armchair configurations) has been considered as the best and direct way to comprehend the nature of metal-free catalysis.

This review thus forecasts a bright future in catalysis by UNDD family materials and the use of unconventional concepts of active sites such as C atoms and C–C bonds with specific charge density due to the presence of nearby heteroatoms, defects or vacancies, and curvature in the graphene-like plane. It is an emerging and conceptually new area of catalytic materials. However, as shown above, there is still a lot of work to be done before this fascinating class of nanocarbons can be brought to light for real practical applications.

## Acronyms

AC	Activated carbon
AOP	Advanced oxidation process
BCDI	Bragg coherent X-ray diffraction imaging
BDD	Boron-doped diamond
BNND	Boron and nitrogen co-doped diamond
BND	Bucky nanodiamond
900 BND	Annealing nanodiamond at 900 °C
1100 BND	Annealing nanodiamond at 1100 °C
1200 BND	Annealing nanodiamond at 1200 °C
1300 BND	Annealing nanodiamond at 1300 °C
CMD	Catalytic methane decomposition
CNT	Carbon nanotube
CRR	CO <sub>2</sub> reduction reaction
CV	Cyclic voltammetry
CVD	Chemical vapour deposition
DFT	Density functional theory
DH	Direct dehydrogenation
DRIFT	Diffuse-reflectance infrared Fourier transform
EB	Ethylbenzene
EELS	Electron energy loss spectroscopy
ESR	Electron spin resonance
ET	Electron transfer
NEXAFS	Near extended X-ray absorption fine structure
FTIR	Fourier transform infrared spectrum
GR	Reduced graphite oxide
GO	Graphite oxide
HOPG	Highly ordered pyrolytic graphite
HRTEM	High-resolution transmission electron microscopy
MOF	Metal–organic framework
MWCNT	Multi-walled carbon nanotube
ND	Nanodiamond
NDD	Nitrogen-doped diamond
N-BND	Nitrogen-modified BND
NMR	Nuclear magnetic resonance
N-OLC	Nitrogen-doped OLC
ODH	Oxidative dehydrogenation
OLC	Onion-like carbon
ORR	Oxygen reduction reaction
PAH	Polycyclic aromatic hydrocarbon
PCET	Proton coupled electron transfer
PDDA	Poly(diallyldimethylammoniumchloride)
PEM	Proton-exchange membrane
PMS	Peroxymonosulfate
PDS	Peroxydisulfate
RDE	Rotating disk electrode
RDS	Rate-determining step
SIMS	Secondary-ion mass spectrometry
SWCNT	Single-walled carbon nanotube
TBHP	<i>tert</i> -Butyl hydroperoxide
TGA	Thermogravimetric analysis
TPD	Temperature programmed desorption
UNDDs	Ultradispersed nanodiamonds and their derivatives





UPS	Ultraviolet photoelectron spectroscopy
XRD	X-ray diffraction
XPS	X-ray photoelectron spectroscopy

## Conflicts of interest

There are no conflicts to declare.

## Acknowledgements

The authors thank Dr Jian Zhang, Xi Liu, Robert Schlögl and Linhui Yu for their great contributions to this study. The authors thank Kuang-Hsu Wu (University of New South Wales) for his comments on this review. The authors thank Dr Vadym N. Mochalin (Missouri University of Science & Technology) and Prof. Y. Gogotsi (Department of Materials Science and Engineering and A. J. Drexel Nanotechnology Institute, Drexel University) for providing the original schematic model of nanodiamond. YL, XS and DS acknowledge the “Strategic Priority Research Program” of the Chinese Academy of Sciences, Grant No. XDA09030103. GC and SP acknowledge the Italian MIUR through the PRIN Project 2015K7FZLH SMARTNESS “Solar driven chemistry: new materials for photo- and electro-catalysis”. Open Access funding provided by the Max Planck Society.

## References

- 1 X. Liu and L. Dai, *Nat. Rev. Mater.*, 2016, **1**, 16064.
- 2 S. Navalón, A. Dhakshinamoorthy, M. Alvaro, M. Antonietti and H. Garcia, *Chem. Soc. Rev.*, 2017, **46**, 4501.
- 3 S. Navalón, J. R. Herance, M. Alvaro and H. Garcia, *Mater. Horiz.*, 2018, **5**, 363.
- 4 X.-H. Li and M. Antonietti, *Chem. Soc. Rev.*, 2013, **42**, 6593.
- 5 Y. Yan, J. Miao, Z. Yang, F.-X. Xiao, H. B. Yang, B. Liu and Y. Yang, *Chem. Soc. Rev.*, 2015, **44**, 3295.
- 6 S. A. Miners, G. A. Rance and A. N. Khlobystov, *Chem. Soc. Rev.*, 2016, **45**, 4727.
- 7 X.-K. Kong, C.-L. Chen and Q.-W. Chen, *Chem. Soc. Rev.*, 2014, **43**, 2841.
- 8 Y. Xu, M. Kraft and R. Xu, *Chem. Soc. Rev.*, 2016, **45**, 3039.
- 9 X. Fan, G. Zhang and F. Zhang, *Chem. Soc. Rev.*, 2015, **44**, 3023.
- 10 W. Qi, P. Yan and D. S. Su, *Acc. Chem. Res.*, 2018, **51**, 640.
- 11 M. R. Benziger, S. N. Talapaneni, S. Joseph, K. Ramadass, G. Singh, J. Scaranto, U. Ravon, K. Al-Bahily and A. Vinu, *Chem. Soc. Rev.*, 2018, **47**, 2680.
- 12 G. Centi and S. Perathoner, *Catal. Today*, 2010, **150**, 151.
- 13 B. Qiu, M. Xing and J. Zhang, *Chem. Soc. Rev.*, 2018, **47**, 2165.
- 14 M.-M. Titirici, R. J. White, N. Brun, V. L. Budarin, D. S. Su, F. del Monte, J. H. Clark and M. J. MacLachlan, *Chem. Soc. Rev.*, 2015, **44**, 250.
- 15 D. S. Su, S. Perathoner and G. Centi, *Chem. Rev.*, 2013, **113**, 5782.
- 16 J. Li, Z. Zhao, Y. Ma and Y. Qu, *ChemCatChem*, 2017, **9**, 1554.
- 17 C. Genovese, C. Ampelli, S. Perathoner and G. Centi, *J. Energy Chem.*, 2013, **22**, 202.
- 18 A. Primo, V. Parvulescu and H. Garcia, *J. Phys. Chem. Lett.*, 2017, **8**, 264.
- 19 E. Perez-Mayoral, V. Calvino-Casilda and E. Soriano, *Catal. Sci. Technol.*, 2016, **6**, 1265.
- 20 G. Centi, S. Perathoner and D. S. Su, *Catal. Surv. Asia*, 2014, **18**, 149.
- 21 M. Li, F. Xu, H. Li and Y. Wang, *Catal. Sci. Technol.*, 2016, **6**, 3670.
- 22 J. Zhang and L. Dai, *ACS Catal.*, 2015, **5**, 7244.
- 23 E. Lam and J. H. T. Luong, *ACS Catal.*, 2014, **4**, 3393.
- 24 W. Qi and D. S. Su, *ACS Catal.*, 2014, **4**, 3212.
- 25 A. Sarapuu, E. Kibena-Poldsepp, M. Borghei and K. Tammeveski, *J. Mater. Chem. A*, 2018, **6**, 776.
- 26 C. Tang and Q. Zhang, *Adv. Mater.*, 2017, **29**, 1604103.
- 27 G. Centi and S. Perathoner, *ChemSusChem*, 2011, **4**, 913.
- 28 D. S. Su and G. Centi, *J. Energy Chem.*, 2013, **22**, 151.
- 29 C. Ampelli, S. Perathoner and G. Centi, *Chin. J. Catal.*, 2014, **35**, 783.
- 30 D. S. Su, S. Perathoner and G. Centi, *Catal. Today*, 2012, **186**, 1.
- 31 D.-W. Wang and D. S. Su, *Energy Environ. Sci.*, 2014, **7**, 576.
- 32 B. Frank, in *Nanocarbon-Inorganic Hybrids*, ed. D. Eder and R. Schlögl, De Gruyter, 2014, p. 393.
- 33 R. Schlögl, *Adv. Catal.*, 2013, **56**, 103.
- 34 D. S. Su and R. Schlögl, *ChemSusChem*, 2010, **3**, 136.
- 35 D. S. Su, J. Zhang, B. Frank, A. Thomas, X. Wang, J. Paraknowitsch and R. Schlögl, *ChemSusChem*, 2010, **3**, 169.
- 36 P. Lanzafame, S. Abate, C. Ampelli, C. Genovese, R. Passalacqua, G. Centi and S. Perathoner, *ChemSusChem*, 2017, **10**, 4409.
- 37 S. Perathoner, S. Gross, E. J. M. Hensen, H. Wessel, H. Chraye and G. Centi, *ChemCatChem*, 2017, **9**, 904.
- 38 S. Abate, K. Barbera, G. Centi, P. Lanzafame and S. Perathoner, *Catal. Sci. Technol.*, 2016, **6**, 2485.
- 39 T. Zhang, Y. Zhu and J. Y. Lee, *J. Mater. Chem. A*, 2018, **6**, 8147.
- 40 L. Liu, Y.-P. Zhu, M. Su and Z.-Y. Yuan, *ChemCatChem*, 2015, **7**, 2765.
- 41 D. Yu, E. Nagelli, F. Du and L. Dai, *J. Phys. Chem. Lett.*, 2010, **1**, 2165.
- 42 Q. Wu, L. Yang, X. Wang and Z. Hu, *Acc. Chem. Res.*, 2017, **50**, 435.
- 43 V. Georgakilas, J. A. Perman, J. Tucek and R. Zboril, *Chem. Rev.*, 2015, **115**, 4744.
- 44 H. Tang, C. M. Hessel, J. Wang, N. Yang, R. Yu, H. Zhao and D. Wang, *Chem. Soc. Rev.*, 2014, **43**, 4281.
- 45 K. Dirian, M. A. Herranz, G. Katsukis, J. Malig, L. Rodriguez-Perez, C. Romero-Nieto, V. Strauss, N. Martin and D. M. Guldi, *Chem. Sci.*, 2013, **4**, 4335.
- 46 L.-F. Chen, Y. Feng, H.-W. Liang, Z.-Y. Wu and S.-H. Yu, *Adv. Energy Mater.*, 2017, **7**, 1700826.



- 47 H. Jiang, P. S. Lee and C. Li, *Energy Environ. Sci.*, 2013, **6**, 41.
- 48 T. F. Liu, S. Ali, Z. Lian, B. Li and D. S. Su, *J. Mater. Chem. A*, 2017, **5**, 21596.
- 49 C. Hu and L. Dai, *Angew. Chem., Int. Ed.*, 2016, **55**, 11736.
- 50 Y. Zhang, J. Zhang and D. S. Su, *ChemSusChem*, 2014, **7**, 1240.
- 51 K. N. Wood, R. O'Hayre and S. Pylypenko, *Energy Environ. Sci.*, 2014, **7**, 1212.
- 52 J. Zhu, A. Holmen and D. Chen, *ChemCatChem*, 2013, **5**, 378.
- 53 G. Tuci, A. Rossin, L. Luconi, C. Pham-Huu, S. Cicchi, H. Ba and G. Giambastiani, *Catal. Sci. Technol.*, 2017, **7**, 5833.
- 54 G. Tuci, C. Zafferoni, A. Rossin, L. Luconi, A. Milella, M. Ceppatelli, M. Innocenti, Y. Liu, C. Pham-Huu and G. Giambastiani, *Catal. Sci. Technol.*, 2016, **6**, 6226.
- 55 G. Tuci, C. Zafferoni, P. D'Ambrosio, S. Caporali, M. Ceppatelli, A. Rossin, T. Tsoufis, M. Innocenti and G. Giambastiani, *ACS Catal.*, 2013, **3**, 2108.
- 56 R. Lv, E. Cruz-Silva and M. Terrones, *ACS Nano*, 2014, **8**, 4061.
- 57 H. Wang and H. Dai, *Chem. Soc. Rev.*, 2013, **42**, 3088.
- 58 G. Centi and S. Perathoner, in *Nanocarbon-Inorganic Hybrids*, ed. D. Eder and R. Schlögl, De Gruyter, 2014, p. 429.
- 59 Y. Cheng, Y. Fan, Y. Pei and M. Qiao, *Catal. Sci. Technol.*, 2015, **5**, 3903.
- 60 D. Zhang, W. Chen, Z. Li, Y. Chen, L. Zheng, Y. Gong, Q. Li, R. Shen, Y. Han, W.-C. Cheong, L. Gu and Y. Li, *Chem. Commun.*, 2018, **54**, 4274.
- 61 Y. Chen, T. Kasama, Z. Huang, P. Hu, J. Chen, X. Liu and X. Tang, *Chem. – Eur. J.*, 2015, **21**, 17397.
- 62 G. Vilé, D. Albani, M. Nachttegaal, Z. Chen, D. Dontsova, M. Antonietti, N. López and J. Pérez-Ramírez, *Angew. Chem., Int. Ed.*, 2015, **54**, 11265.
- 63 H. Fei, J. Dong, M. J. Arellano-Jiménez, G. Ye, N. D. Kim, E. L. Samuel, Z. Peng, Z. Zhu, F. Qin and J. Bao, *Nat. Commun.*, 2015, **6**, 8668.
- 64 H.-W. Liang, S. Brüller, R. Dong, J. Zhang, X. Feng and K. Müllen, *Nat. Commun.*, 2015, **6**, 7992.
- 65 G. Zhao, H. Liu and J. Ye, *Nano Today*, 2018, **19**, 108.
- 66 D. Liu, C. Wu, S. Chen, S. Ding, Y. Xie, C. Wang, T. Wang, Y. A. Haleem, Z. ur Rehman, Y. Sang, Q. Liu, X. Zheng, Y. Wang, B. Ge, H. Xu and L. Song, *Nano Res.*, 2018, **11**, 2217.
- 67 L.-L. Liu, C.-P. Chen, L.-S. Zhao, Y. Wang and X.-C. Wang, *Carbon*, 2017, **115**, 773.
- 68 S. Navalon, A. Dhakshinamoorthy, M. Alvaro and H. Garcia, *Chem. Rev.*, 2014, **114**, 6179.
- 69 D. Guo, R. Shibuya, C. Akiba, S. Saji, T. Kondo and J. Nakamura, *Science*, 2016, **351**, 361.
- 70 S. Perathoner, C. Ampelli, S. Chen, R. Passalacqua, D. Su and G. Centi, *J. Energy Chem.*, 2017, **26**, 207.
- 71 C. Su and K. P. Loh, *Acc. Chem. Res.*, 2013, **46**, 2275.
- 72 P. Tang, G. Hu, M. Li and D. Ma, *ACS Catal.*, 2016, **6**, 6948.
- 73 M. Shao, Q. Chang, J.-P. Dodelet and R. Chenitz, *Chem. Rev.*, 2016, **116**, 3594.
- 74 C. K. Chua and M. Pumera, *Chem. – Eur. J.*, 2015, **21**, 12550.
- 75 L. Dai, Y. Xue, L. Qu, H.-J. Choi and J.-B. Baek, *Chem. Rev.*, 2015, **115**, 4823.
- 76 H. Hu, J. H. Xin, H. Hu, X. Wang and Y. Kong, *Appl. Catal., A*, 2015, **492**, 1.
- 77 N. Matsumoto, L. Joly-Pottuz, H. Kinoshita and N. Ohmae, *Diamond Relat. Mater.*, 2007, **16**, 1227.
- 78 J. Zang, Y. Wang, L. Bian, J. Zhang, F. Meng, Y. Zhao, X. Qu and S. Ren, *Int. J. Hydrogen Energy*, 2012, **37**, 6349.
- 79 M. Chen, X.-Q. Zhang, H. B. Man, R. Lam, E. K. Chow and D. Ho, *J. Phys. Chem. Lett.*, 2010, **1**, 3167.
- 80 Y.-R. Chang, H.-Y. Lee, K. Chen, C.-C. Chang, D.-S. Tsai, C.-C. Fu, T.-S. Lim, Y.-K. Tzeng, C.-Y. Fang, C.-C. Han, H.-C. Chang and W. Fann, *Nat. Nanotechnol.*, 2008, **3**, 284.
- 81 V. N. Mochalin, O. Shenderova, D. Ho and Y. Gogotsi, *Nat. Nanotechnol.*, 2012, **7**, 11.
- 82 Z. R. Dai, J. P. Bradley, D. J. Joswiak, D. E. Brownlee, H. G. M. Hill and M. J. Genge, *Nature*, 2002, **418**, 157.
- 83 V. V. Danilenko, *Phys. Solid State*, 2004, **46**, 595.
- 84 N. R. Johnson, N. R. Greiner, D. S. Phillips, J. D. Johnson and F. Volk, *Nature*, 1988, **333**, 440.
- 85 V. L. Kuznetsov, A. L. Chuvilin, E. M. Moroz, V. N. Kolomiichuk, S. K. Shaikhutdinov, Y. V. Butenko and I. Y. Mal'kov, *Carbon*, 1994, **32**, 873.
- 86 S. Osswald, G. Yushin, V. Mochalin, S. O. Kucheyev and Y. Gogotsi, *J. Am. Chem. Soc.*, 2006, **128**, 11635.
- 87 O. O. Mykhaylyk and Y. M. Solonin, *J. Appl. Phys.*, 2005, **97**, 074302.
- 88 D. Pech, M. Brunet, H. Durou, P. Huang, V. Mochalin, Y. Gogotsi, P.-L. Taberna and P. Simon, *Nat. Nanotechnol.*, 2010, **5**, 651.
- 89 M. Zeiger, N. Jackel, V. N. Mochalin and V. Presse, *J. Mater. Chem. A*, 2016, **4**, 3172.
- 90 M. Li, W. Liu, H. Zhang, Z. Liang, P. Duan, X. Yan, P. Guan, B. Xu and J. Guo, *Phys. Chem. Chem. Phys.*, 2018, **20**, 2022.
- 91 T. Petit, J.-C. Arnault, H. A. Girard, M. Sennour and P. Bergonzo, *Phys. Rev. B: Condens. Matter Mater. Phys.*, 2011, **84**, 233407.
- 92 V. L. Kuznetsov, I. L. Zilberberg, Yu. V. Butenko and A. L. Chuvilin, *J. Appl. Phys.*, 1999, **86**, 863.
- 93 F. Ding and B. I. Yakobson, *J. Phys. Chem. Lett.*, 2014, **5**, 2922.
- 94 S. O. Hruszkewycz, W. Cha, P. Andrich, C. P. Anderson, A. Ulvestad, R. Harder, P. H. Fuoss, D. D. Awschalom and F. J. Heremans, *APL Mater.*, 2017, **5**, 026105.
- 95 V. L. Kuznetsov, A. L. Chuvilin, Y. V. Butenko, I. Y. Mal'kov and V. M. Titov, *Chem. Phys. Lett.*, 1994, **222**, 343.
- 96 L. Hawelek, A. Brodka, S. Tomita, J. C. Dore, V. Honkimäki and A. Burian, *Diamond Relat. Mater.*, 2011, **20**, 1333.
- 97 M. Todt, R. D. Bitsche, M. A. Hartmann, F. D. Fischer and F. G. Rammerstorfer, *Int. J. Solids Struct.*, 2014, **51**, 706.
- 98 J.-F. Cui, X.-W. Fang and K. Schmidt-Rohr, *J. Phys. Chem. C*, 2014, **118**, 9621.
- 99 Y. Lin, Z. Feng, L. Yu, Q. Gu, S. Wu and D. S. Su, *Chem. Commun.*, 2017, **53**, 4834.

- 100 Y. V. Butenko, V. L. Kuznetsov, E. A. Paukshtis, A. I. Stadnichenko, I. N. Mazov, S. I. Moseenkov, A. I. Boronin and S. V. Kosheev, *Fullerenes, Nanotubes, Carbon Nanostruct.*, 2006, **14**, 557.
- 101 G. P. Bogatyreva, M. A. Marinich, E. V. Ishchenko, V. L. Gvyazdovskaya, G. A. Bazalii and N. A. Oleinik, *Phys. Solid State*, 2004, **46**, 738.
- 102 B. Moosa, K. Fhayli, S. Li, K. Julfakyan, A. Ezzeddine and N. M. Khashab, *J. Nanosci. Nanotechnol.*, 2014, **14**, 332.
- 103 V. L. Kuznetsov, M. N. Aleksandrov, I. V. Zagoruiko, A. L. Chuvilin, E. M. Moroz, V. N. Kolomiichuk, V. A. Likholobov, P. M. Brylyakov and G. V. Sakovitchet, *Carbon*, 1991, **29**, 665.
- 104 A. S. Barnard, S. P. Russo and I. K. Snook, *Phys. Rev. B: Condens. Matter Mater. Phys.*, 2003, **68**, 073406.
- 105 G. C. C. Costa, J. K. McDonough, Y. Gogotsi and A. Navrotsky, *Carbon*, 2014, **69**, 490.
- 106 S. Tomita, T. Sakurai, H. Ohta, M. Fujii and S. Hayashi, *J. Chem. Phys.*, 2001, **114**, 7477.
- 107 L. G. Bulusheva, A. V. Okotrub, V. L. Kuznetsov, A. L. Chuvilin, Y. V. Butenko and M. I. Heggie, *MRS Proc.*, 2002, **703**, V9.22.
- 108 D. Holec, M. A. Hartmann, F. D. Fischer, F. G. Rammerstorfer, P. H. Mayrhofer and O. Paris, *Phys. Rev. B: Condens. Matter Mater. Phys.*, 2010, **81**, 235403.
- 109 E. M. Zagrebina, A. V. Generalov, A. Yu. Klyushin, K. A. Simonov, N. A. Vinogradov, M. Dubois, L. Frezet, N. Martensson, A. B. Preobrajenski and A. S. Vinogradov, *J. Phys. Chem. C*, 2015, **119**, 835.
- 110 D. S. Sutar, G. Singh and V. D. Botcha, *Appl. Phys. Lett.*, 2012, **101**, 103103.
- 111 S. H. Lim, H. I. Elim, X. Y. Gao, A. T. S. Wee, W. Ji, J. Y. Lee and J. Lin, *Phys. Rev. B: Condens. Matter Mater. Phys.*, 2006, **73**, 045402.
- 112 M. Shiraishi and M. Ata, *Carbon*, 2001, **39**, 1913.
- 113 H. Ago, T. Kugler, F. Cacialli, W. R. Salaneck, M. S. P. Shaffer, A. H. Windle and R. H. Friend, *J. Phys. Chem. B*, 1999, **103**, 8116.
- 114 A. Siokou, F. Ravani, S. Karakalos, O. Frank, M. Kalbac and C. Galiotis, *Appl. Surf. Sci.*, 2011, **257**, 9785.
- 115 M. Shiraishi and M. Ata, *Mater. Res. Soc. Symp. Proc.*, 2001, **72**, 633.
- 116 X. Li, X. Pan, L. Yu, P. Ren, X. Wu, L. Sun, F. Jiao and X. Bao, *Nat. Commun.*, 2014, **5**, 3688.
- 117 J. Zhang, X. Liu, R. Blume, A. Zhang, R. Schlogl and D. S. Su, *Science*, 2008, **322**, 73.
- 118 B. Dai, K. Chen, Y. Wang, L. Kang and M. Zhu, *ACS Catal.*, 2015, **5**, 2541.
- 119 A. Schüle, U. Nieken, O. Shekhah, W. Ranke, R. Schlögl and G. Kolios, *Phys. Chem. Chem. Phys.*, 2007, **9**, 3619.
- 120 J. H. B. S. Jesper, R.-M. Javier, S.-J. Eduardo and M. W. Bert, *Chem. Rev.*, 2014, **114**, 10613.
- 121 N. Keller, N. I. Maksimova, V. V. Roddatis, M. Schur, G. Mestl, Y. V. Butenko, V. L. Kuznetsov and R. Schlögl, *Angew. Chem., Int. Ed.*, 2002, **41**, 1885.
- 122 D. S. Su, N. Maksimova, J. J. Delgado, N. Keller, G. Mestl, M. J. Ledoux and R. Schlögl, *Catal. Today*, 2005, **102–103**, 110.
- 123 J. Zhang, D. S. Su, A. Zhang, D. Wang, R. Schlögl and C. Hebert, *Angew. Chem., Int. Ed.*, 2007, **46**, 7319.
- 124 D. S. Su, N. I. Maksimova, G. Mestl, V. L. Kuznetsov, V. Keller, R. Schlögl and N. Keller, *Carbon*, 2007, **45**, 2145.
- 125 J. Zhang, D. S. Su, R. Blume, R. Schlögl, R. Wang, X. Yang and A. Gajovic, *Angew. Chem., Int. Ed.*, 2010, **49**, 8640.
- 126 X. Liu, B. Frank, W. Zhang, T. P. Cotter, R. Schlögl and D. S. Su, *Angew. Chem., Int. Ed.*, 2011, **50**, 3318.
- 127 X. Sun, R. Wang, B. Zhang, R. Huang, X. Huang, D. S. Su, T. Chen, C. Miao and W. Yang, *ChemCatChem*, 2014, **6**, 2270.
- 128 R. Wang, X. Y. Sun, B. S. Zhang, X. Y. Sun and D. S. Su, *Chem. – Eur. J.*, 2014, **20**, 6324.
- 129 X. Sun, Y. Ding, B. Zhang, R. Huang, D. Chen and D. S. Su, *ACS Catal.*, 2015, **5**, 2436.
- 130 X. Sun, Y. Ding, B. Zhang, R. Huang and D. S. Su, *Chem. Commun.*, 2015, **51**, 9145.
- 131 B. Zhong, J. Zhang, B. Li, B. Zhang, C. Dai, X. Sun, R. Wang and D. S. Su, *Phys. Chem. Chem. Phys.*, 2014, **16**, 4488.
- 132 U. P. M. Ashik, W. M. A. Wan Daud and H. F. Abbas, *Renewable Sustainable Energy Rev.*, 2015, **44**, 221.
- 133 R. Guil-Lopez, J. A. Botas, J. L. G. Fierro and D. P. Serrano, *Appl. Catal., A*, 2011, **396**, 40.
- 134 N. Q. Zhao, C. N. He, J. Ding, T. C. Zou, Z. J. Qiao, C. S. Shi, X. W. Du, J. J. Li and Y. D. Li, *J. Alloys Compd.*, 2007, **428**, 79.
- 135 R. Aiello, J. E. Fiscus, H.-C. Zur Loye and M. D. Amiridis, *Appl. Catal., A*, 2000, **192**, 227.
- 136 J. Diao, Z. Feng, R. Huang, H. Liu, S. B. A. Hamid and D. S. Su, *ChemSusChem*, 2016, **9**, 662.
- 137 G. C. Grunewald and R. S. Drago, *J. Mol. Catal.*, 1990, **58**, 227.
- 138 B. Frank, M. Morassutto, R. Schomäcker, R. Schlögl and D. S. Su, *ChemCatChem*, 2010, **2**, 644.
- 139 B. Frank, J. Zhang, R. Blume, R. Schlögl and D. S. Su, *Angew. Chem., Int. Ed.*, 2009, **48**, 6913.
- 140 C. L. Chen, J. Zhang, B. S. Zhang, C. L. Yu, F. Peng and D. S. Su, *Chem. Commun.*, 2013, **49**, 8151.
- 141 V. Schwartz, H. Xie, H. M. Meyer, S. H. Overbury and C. D. Liang, *Carbon*, 2011, **49**, 659.
- 142 F. Cavani, N. Ballarini and A. Cericola, *Catal. Today*, 2007, **127**, 113.
- 143 H. Y. Liu, J. Y. Diao, Q. Wang, S. Y. Gu, T. Chen, C. X. Miao, W. M. Yang and D. S. Su, *Chem. Commun.*, 2014, **50**, 7810.
- 144 H. Ba, Y. Liu, X. Mu, W. H. Doh, J. M. Nhuta, P. Granger and C. Pham-Huu, *Appl. Catal., A*, 2015, **499**, 217.
- 145 J. Diao, H. Liu, Z. Feng, Y. Zhang, T. Chen, C. Miao, W. Yang and D. S. Su, *Catal. Sci. Technol.*, 2015, **5**, 4950.
- 146 H. Ba, S. Podila, Y. Liu, X. Mu, J. M. Nhuta, V. Papaefthimiou, S. Zafeiratos, P. Granger and C. Pham-Huu, *Catal. Today*, 2015, **249**, 167.
- 147 Z. Zhao, Y. Dai, G. Ge, Q. Mao, Z. Rong and G. Wang, *ChemCatChem*, 2015, **7**, 1070.
- 148 T. T. Thanh, H. Ba, T. P. Lai, J. M. Nhut, O. Ersen, D. Begin, I. Janowska, D. L. Nguyen, P. Granger and C. Pham-Huu, *J. Mater. Chem. A*, 2014, **2**, 11349.





- 149 H. Ba, L. Truong-Phuoc, Y. Liu, C. Duong-Viet, J.-M. Nhut, L. Nguyen-Dinh, P. Granger and C. Pham-Huu, *Carbon*, 2016, **96**, 1060.
- 150 Z. K. Zhao and Y. T. Dai, *J. Mater. Chem. A*, 2014, **2**, 13442.
- 151 Z. Zhao, W. Li, Y. Dai, G. Ge, X. Guo and G. Wang, *ACS Sustainable Chem. Eng.*, 2015, **3**, 3355.
- 152 L. Roldán, A. M. Benito and E. García-Bordejé, *J. Mater. Chem. A*, 2015, **3**, 24379.
- 153 D. Su, G. Wen, S. Wu, F. Peng and R. Schlögl, *Angew. Chem., Int. Ed.*, 2017, **56**, 936.
- 154 F. Cavani, G. Centi, S. Perathoner and F. Trifirò, *Sustainable Industrial Chemistry: Principles, Tools and Industrial Examples*, Wiley-VCH, 2009.
- 155 G. Centi and R. A. van Santen, *Catalysis for Renewables: From Feedstock to Energy Production*, Wiley-VCH, 2007.
- 156 Y. Lin and D. Su, *ACS Nano*, 2014, **8**, 7823.
- 157 S. C. Laha and R. Kumar, *J. Catal.*, 2001, **204**, 64.
- 158 X. Deng and C. M. Friend, *J. Am. Chem. Soc.*, 2005, **127**, 17178.
- 159 Y. Lin, X. Pan, W. Qi, B. Zhang and D. S. Su, *J. Mater. Chem. A*, 2014, **2**, 12475.
- 160 J. Huang, C. Liu, D. Sun, Y. Hong, M. Du, T. Odoom-Wubah, W. Fang and Q. Li, *Chem. Eng. J.*, 2014, **235**, 215.
- 161 R. Ghosh, X. Shen, J. C. Villegas, Y. Ding, K. Malinger and S. L. Suib, *J. Phys. Chem. B*, 2006, **110**, 7592.
- 162 Y. Gao, G. Hu, J. Zhong, Z. Shi, Y. Zhu, D. S. Su, J. Wang, X. Bao and D. Ma, *Angew. Chem., Int. Ed.*, 2013, **52**, 2109.
- 163 Y. Lin, B. Li, Z. Feng, Y. A. Kim, M. Endo and D. S. Su, *ACS Catal.*, 2015, **5**, 5921.
- 164 Y. Lin, K.-H. Tim Wu, L. Yu, S. Heumann and D. S. Su, *ChemSusChem*, 2017, **10**, 3497.
- 165 A. S. Stasinakis, *Global NEST J.*, 2008, **10**, 376.
- 166 W.-D. Oh, Z. I. Dong and T.-T. Lim, *Appl. Catal., B*, 2016, **194**, 169.
- 167 X. Duan, Z. Ao, L. Zhou, H. Sun, G. Wang and S. Wang, *Appl. Catal., B*, 2016, **188**, 98.
- 168 X. Duan, C. Su, L. Zhou, H. Sun, A. Suvorova, T. Odedairo, Z. Zhu, Z. Shao and S. Wang, *Appl. Catal., B*, 2016, **194**, 7.
- 169 H. Lee, H.-i Kim, S. Weon, W. Choi, Y. S. Hwang, J. Seo, C. Lee and J.-H. Kim, *Environ. Sci. Technol.*, 2016, **50**, 10134.
- 170 X. Duan, Z. Aob, H. Zhang, M. Saunders, H. Sund, Z. Shao and S. Wang, *Appl. Catal., B*, 2018, **222**, 176.
- 171 X. Duan, Z. Ao, D. Li, H. Sun, L. Zhou, A. Suvorova, M. Saunders, G. Wang and S. Wang, *Carbon*, 2016, **103**, 404.
- 172 A. Corma and P. Serna, *Science*, 2006, **313**, 332.
- 173 R. V. Jagadeesh, A. E. Surkus, H. Junge, M. M. Pohl, J. Radnik, J. Rabeah, H. Huan, V. Schunemann, A. Bruckner and M. Beller, *Science*, 2013, **342**, 1073.
- 174 Y. Lin, S. Wu, W. Shi, B. Zhang, J. Wang, Y. A. Kim, M. Endo and D. S. Su, *Chem. Commun.*, 2015, **51**, 13086.
- 175 Q. Zhang, Y. Liu, S. Chen, X. Quan and H. Yu, *J. Hazard. Mater.*, 2014, **265**, 185.
- 176 W. S. Yeap, S. Chen and K. P. Loh, *Chem. Mater.*, 2009, **25**, 185.
- 177 X. Sun, R. Wang and D. Su, *Chin. J. Catal.*, 2013, **34**, 508.
- 178 E. Y. Choi and C. K. Kim, *Sci. Rep.*, 2017, **7**, 4178.
- 179 K. Chatterjee, M. Ashokkumar, H. Gullapalli, Y. Gong, R. Vajtai, P. Thanikaivelan and P. M. Ajayan, *Carbon*, 2018, **130**, 645.
- 180 Y. Liu, S. Chen, X. Quan, H. Yu, H. Zhao, Y. Zhang and G. Chen, *J. Phys. Chem. C*, 2013, **117**, 14992.
- 181 Y. Zhu, Y. Lin, B. Zhang, J. Rong, B. Zong and D. S. Su, *ChemCatChem*, 2015, **7**, 2840.
- 182 N. Kannari, T. Itakura and J. Ozaki, *Carbon*, 2015, **87**, 415.
- 183 L. Dong, J. Zang, J. Su, Y. Jia, Y. Wang, J. Lu and X. Xu, *Electrochim. Acta*, 2015, **174**, 1017.
- 184 D. M. Jang, H. S. Im, S. H. Back, K. Park, Y. R. Lim, C. S. Jung, J. Park and M. Lee, *Phys. Chem. Chem. Phys.*, 2014, **16**, 2411.
- 185 R. Liu, D. Wu, X. Feng and K. Müllen, *Angew. Chem.*, 2010, **122**, 2619.
- 186 D. Geng, Y. Chen, Y. Chen, Y. Li, R. Li, X. Sun, S. Ye and S. Knights, *Energy Environ. Sci.*, 2011, **4**, 760.
- 187 Y. Zhang, A. Reed and D. Y. Kim, *Curr. Appl. Phys.*, 2018, **18**, 417.
- 188 Y. Lin, Y. Zhu, B. Zhang, Y. A. Kim, M. Endo and D. S. Su, *J. Mater. Chem. A*, 2015, **3**, 21805.
- 189 N. Suo, H. Huang, A. Wu, G. Cao, X. Hou and G. Zhang, *Appl. Surf. Sci.*, 2018, **439**, 329.
- 190 X. Sun, J. Xu, Y. Ding, B. Zhang, Z. Feng and D. S. Su, *ChemSusChem*, 2015, **8**, 2872.
- 191 X. Liu, Y. Wang, L. Dong, X. Chen, G. Xin, Y. Zhang and J. Zang, *Electrochim. Acta*, 2016, **194**, 161.
- 192 J. Koh, S. H. Park, M. W. Chung, S. Y. Lee and S. I. Woo, *RSC Adv.*, 2016, **6**, 27528.
- 193 K. Gong, F. Du, Z. Xia, M. Durstock and L. Dai, *Science*, 2009, **323**, 760.
- 194 X. Hu, Y. Wu, H. Li and Z. Zhang, *J. Phys. Chem. C*, 2010, **114**, 9603.
- 195 S. Ni, Z. Li and J. Yang, *Nanoscale*, 2012, **4**, 1184.
- 196 L. Yang, S. Jiang, Y. Zhao, L. Zhu, S. Chen, X. Wang, Q. Wu, J. Ma, Y. Ma and Z. Hu, *Angew. Chem., Int. Ed.*, 2011, **50**, 7132.
- 197 Y. Zhao, L. Yang, S. Chen, X. Wang, Y. Ma, Q. Wu, Y. Jiang, W. Qian and Z. Hu, *J. Am. Chem. Soc.*, 2013, **135**, 1201.
- 198 A. Shen, Y. Zou, Q. Wang, R. A. W. Dryfe, X. Huang, S. Dou, L. Dai and S. Wang, *Angew. Chem.*, 2014, **126**, 10980.
- 199 L. Tao, Q. Wang, S. Dou, Z. Ma, J. Huo, S. Wang and L. Dai, *Chem. Commun.*, 2016, **52**, 2764.
- 200 G. Centi, E. A. Quadrelli and S. Perathoner, *Energy Environ. Sci.*, 2013, **6**, 1711.
- 201 E. A. Quadrelli, G. Centi, J. L. Duplan and S. Perathoner, *ChemSusChem*, 2011, **4**, 1194.
- 202 C. Ampelli, S. Perathoner and G. Centi, *Philos. Trans. R. Soc., A*, 2015, **373**, 20140177.
- 203 S. Perathoner and G. Centi, *Catal. Today*, 2018, DOI: 10.1016/j.cattod.2018.03.005.
- 204 C. Costentin, M. Robert and J.-M. Savéant, *Chem. Soc. Rev.*, 2013, **42**, 2423.
- 205 K. Nakata, T. Ozaki, C. Terashima, A. Fujishima and Y. Einaga, *Angew. Chem.*, 2014, **126**, 890.
- 206 Y. Liu, S. Chen, X. Quan and H. Yu, *J. Am. Chem. Soc.*, 2015, **137**, 11631.



- 207 Y. Liu, Y. Zhang, K. Cheng, X. Quan, X. Fan, Y. Su, S. Chen, H. Zhao, Y. Zhang, H. Yu and M. R. Hoffmann, *Angew. Chem., Int. Ed.*, 2017, **56**, 15607.
- 208 X. Duan, J. Xu, Z. Wei, J. Ma, S. Guo, S. Wang, H. Liu and S. Dou, *Adv. Mater.*, 2017, **29**, 1701784.
- 209 S. Liu, H. Yang, X. Huang, L. Liu, W. Cai, J. Gao, X. Li, T. Zhang, Y. Huang and B. Liu, *Adv. Funct. Mater.*, 2018, **28**, 1800499.
- 210 J. Xu, Y. Kan, R. Huang, B. Zhang, B. Wang, K. H. Wu, Y. Lin, X. Sun, Q. Li, G. Centi and D. S. Su, *ChemSusChem*, 2016, **9**, 1085.
- 211 Y. Liu, S. Chen, X. Quan, X. Fan, H. Zhao, Q. Zhao and H. Yu, *Appl. Catal., B*, 2014, **154–155**, 206.
- 212 L. H. Chen, J. B. Zang, Y. H. Wang and L. Y. Bian, *Electrochim. Acta*, 2008, **53**, 3442.
- 213 C. Shu, Y. Lin and D. Su, *J. Mater. Chem. A*, 2016, **4**, 2128.
- 214 C. Shu, Y. Lin, B. Zhang, S. B. A. Hamid and D. Su, *J. Mater. Chem. A*, 2016, **4**, 6610.
- 215 A. Fujishima, X. Zhang and D. A. Tryk, *Surf. Sci. Rep.*, 2008, **63**, 515.
- 216 L. Zhang and R. J. Hamers, *Diamond Relat. Mater.*, 2017, **78**, 24.
- 217 D. M. Jang, Y. Myung, H. S. Im, Y. S. Seo, Y. J. Cho, C. W. Lee, J. Park, A.-Y. Jeeb and M. Lee, *Chem. Commun.*, 2012, **48**, 696.
- 218 K. M. Tripathi, T. S. Tran, Y. J. Kim and T. Y. Kim, *ACS Sustainable Chem. Eng.*, 2017, **5**, 3982.
- 219 G. Centi and S. Perathoner, *Comprehensive Inorganic Chemistry II, Section 7.18 "Mixed-Metal Oxides"*, 2014, p. 153.
- 220 Q. Yuan, Z. Xu, B. I. Yakobson and F. Ding, *Phys. Rev. Lett.*, 2012, **108**, 245505.
- 221 J. Kim, A. J. Page, S. Irle and K. Morokuma, *J. Am. Chem. Soc.*, 2012, **134**, 9311.
- 222 K. P. S. S. Hembram and G. M. Rao, *Mater. Lett.*, 2012, **72**, 68.
- 223 J.-C. Charlier, *Acc. Chem. Res.*, 2002, **35**, 1063.
- 224 J. M. Carlsson and M. Scheffler, *Phys. Rev. Lett.*, 2006, **96**, 046806.
- 225 J.-P. Tessonnier, A. Villa, O. Majoulet, D. S. Su and R. Schlögl, *Angew. Chem., Int. Ed.*, 2009, **48**, 6543.
- 226 C.-Y. Chen and C. T. Jafvert, *Energy Environ. Sci.*, 2010, **44**, 6674.
- 227 Y. Luo, Y. Heng, X. Dai, W. Chen and J. Li, *J. Solid State Chem.*, 2009, **182**, 2521.
- 228 C. Su, M. Acik, K. Takai, J. Lu, S. J. Hao, Y. Zheng, P. Wu, Q. Bao, T. Enoki, Y. J. Chabal and K. P. Loh, *Nat. Commun.*, 2012, **3**, 1298.
- 229 G. Centi, M. Gangeri, M. Fiorello, S. Perathoner, J. Amadou, D. Bégin, M. J. Ledoux, C. Pham-Huu, M. E. Schuster, D. S. Su, J.-P. Tessonnier and R. Schlögl, *Catal. Today*, 2009, **147**, 287.
- 230 R. A. Sidik, A. B. Anderson, N. P. Subramanian, S. P. Kumaraguru and B. N. Popov, *J. Phys. Chem. B*, 2006, **110**, 1787.
- 231 H. Kim, K. Lee, S. I. Woo and Y. Jung, *Phys. Chem. Chem. Phys.*, 2011, **13**, 17505.
- 232 K.-H. Wu, D.-W. Wang, D. S. Su and J. R. Gentle, *ChemSusChem*, 2015, **8**, 2772.
- 233 G.-L. Chai, Z. Hou, D.-J. Shu, T. Ikeda and K. Terakura, *J. Am. Chem. Soc.*, 2014, **136**, 13629.
- 234 D. Sh. Sabirov, S. L. Khursan and R. G. Bulgakov, *Russ. Chem. Bull.*, 2008, **57**, 2520.
- 235 J. Yang, Y. Liu, D. Zhang, X. Wang, R. Li and Y. Li, *Nano Res.*, 2015, **8**, 3054.
- 236 M. Anafcheh, Z. Khodadadi, F. Ektefa and R. Ghafouri, *J. Phys. Chem. Solids*, 2016, **92**, 26.
- 237 M. Anafcheh, *Mol. Phys.*, 2018, **116**, 179.
- 238 K. Barbera, L. Frusteri, G. Italiano, L. Spadaro, F. Frusteri, S. Perathoner and G. Centi, *Chin. J. Catal.*, 2014, **35**, 869.
- 239 L. Frusteri, C. Cannilla, G. Bonura, A. L. Chuvilin, S. Perathoner, G. Centi and F. Frusteri, *Catal. Today*, 2016, **277**, 68.
- 240 G. Centi, K. Barbera, S. Perathoner, N. K. Gupta, E. E. Ember and J. A. Lercher, *ChemCatChem*, 2015, **7**, 3036.
- 241 D. J. Appelhans, Z. Lin and M. T. Lusk, *Phys. Rev. B: Condens. Matter Mater. Phys.*, 2010, **82**, 073410.
- 242 T. F. Yeh, C. Y. Teng, S. J. Chen and H. S. Teng, *Adv. Mater.*, 2014, **26**, 3297.
- 243 T. F. Yeh, S. J. Chen and H. S. Teng, *Nano Energy*, 2015, **12**, 476.
- 244 Y. Zhai, Z. Zhu and S. Dong, *ChemCatChem*, 2015, **7**, 2806.
- 245 X. Zhou, J. Qiao, L. Yang and J. Zhang, *Adv. Energy Mater.*, 2014, **4**, 1301523.
- 246 Y. Yang, K. Chiang and N. Burke, *Catal. Today*, 2011, **178**, 197.
- 247 V. Calvino-Casilda, A. J. Lopez-Peinado, C. J. Duran-Valle and R. M. Martin-Aranda, *Catal. Rev.: Sci. Eng.*, 2010, **52**, 325.
- 248 J. J. Vilatela and D. Eder, *ChemSusChem*, 2012, **5**, 456.
- 249 D. Eder, *Chem. Rev.*, 2010, **110**, 1348.
- 250 R. Arrigo, M. E. Schuster, S. Abate, S. Wrabetz, K. Amakawa, D. Teschner, M. Freni, G. Centi, S. Perathoner, M. Hävecker and R. Schlögl, *ChemSusChem*, 2014, **7**, 179.
- 251 S. Abate, M. Freni, R. Arrigo, M. E. Schuster, S. Perathoner and G. Centi, *ChemCatChem*, 2013, **5**, 1899.
- 252 S. Abate, R. Arrigo, M. E. Schuster, S. Perathoner, G. Centi, A. Villa, D. Su and R. Schlögl, *Catal. Today*, 2010, **157**, 280.
- 253 B. Zhang and D. S. Su, *ChemCatChem*, 2015, **16**, 3639.
- 254 B. Zhang, L. Shao, W. Zhang, X. Sun, X. Pan and D. S. Su, *ChemCatChem*, 2014, **6**, 2607.
- 255 S. Chen, S. Perathoner, C. Ampelli, C. Mebrahtu, D. Su and G. Centi, *ACS Sustainable Chem. Eng.*, 2017, **5**, 7393.
- 256 S. Chen, S. Perathoner, C. Ampelli, C. Mebrahtu, D. Su and G. Centi, *Angew. Chem.*, 2017, **129**, 2743.
- 257 C. Genovese, M. E. Schuster, E. K. Gibson, D. Gianolio, V. Posligua, R. Grau-Crespo, G. Cibin, P. P. Wells, D. Garai, V. Solokha, S. K. Calderon, J. J. Velasco-Velez, C. Ampelli, S. Perathoner, G. Held, G. Centi and R. Arrigo, *Nat. Commun.*, 2018, **9**, 935.
- 258 W. Qi, W. Liu, B. Zhang, X. Gu, X. Guo and D. Su, *Angew. Chem., Int. Ed.*, 2013, **52**, 14224.
- 259 X. Guo, W. Qi, W. Liu, P. Yan, F. Li, C. Liang and D. Su, *ACS Catal.*, 2017, **7**, 1424.
- 260 R. Passalacqua, S. Perathoner and G. Centi, *J. Energy Chem.*, 2017, **26**, 219.

